Barkhausen noise hysteresis cycle: Theoretical and experimental understanding

Patrick Fagan, Shurui Zhang, Gaël Sebald, Tetsuya Uchimoto, Benjamin Ducharne

Barkhausen noise hysteresis cycle: theoretical and experimental understanding

Patrick Fagan[1,2], Shurui Zhang[2,3], Gael Sebald[4], Tetsuya Uchimoto[4,5], Benjamin Ducharne[2,4*]

[1] - Université Paris-Saclay, Centrale Supélec, CNRS, Group of Electrical Engineering-Paris (GeePs), 91192, Gif-sur-Yvette, France.
[2] - Univ. Lyon, INSA Lyon, LGEF EA682, Villeurbanne, France.
[3] - Graduate School of Engineering, Tohoku University, Sendai, Japan.
[4] - ELyTMaX IRL3757, CNRS, Univ Lyon, INSA Lyon, Centrale Lyon, Université Claude Bernard Lyon 1, Tohoku University, Sendai, Japan.
[5] - Institute of Fluid Science (IFS), Tohoku University, Sendai, Japan.

* Corresponding author: benjamin.ducharne@insa-lyon.fr

Abstract

Magnetic Barkhausen Noise (MBN) reflects magnetic domains' motions during a ferromagnetic part's magnetization process. For industrial specimens, the raw MBN signal is stochastic and not reproducible, leading to complex analyses. This issue is solved using time-average variables like the Magnetic Barkhausen Noise energy (MBN_{energy}).

Plotting MBN_{energy} as a function of the magnetic excitation gives rise to a hysteresis cycle. Recent studies have highlighted some exciting properties from this cycle, such as a way to observe the magnetic loss contribution associated with the domain wall motions. Still, questions remain, including in the basic description of MBN_{energy}.

This paper describes a theoretical development to understand MBN_{energy} further. We demonstrate that in standard characterization conditions, the magnetization variations associated with the domain wall motions are proportional to the square of the envelope of the MBN signal instead of its absolute value.

Then, this theoretical conclusion is confirmed experimentally. Finally, the absence of privileged orientation and direction in the MBN effect is verified in the case of unidirectional magnetization.

Keywords: Magnetization rotation, directional Barkhausen activity, magnetic losses

Nomenclature

Physical variables		
Symbol	**Name**	**Unit**
S	Cross-section	m^2
H_{surf}	Surface magnetic excitation field	A/m
H_{sat}	Magnetic excitation maximal value	A/m
M	Magnetization	A/m
M_{sat}	Saturation magnetization	A/m
B_a	Magnetic flux density	T
μ_0	Vacuum permeability	A/m
$\mu_{diff\ inc}$	Diff. permeability at the saturation elbow (increasing branch)	A/m
$\mu_{diff\ Hc}$	Diff. permeability at coercivity	A/m
V_{MBN}	Magnetic Barkhausen Noise (MBN) voltage	V
MBN_{energy}	Magnetic Barkhausen Noise energy	$V^{\alpha}\cdot s$
α	Magnetic Barkhausen Noise energy exponent	1
n	Number of turns	1
e	Electromotive force in the sensing coil	V
x_i^{MBN}	i-th element of the MBN cycle array	$V^{\alpha}\cdot s$
x_i^{clas}	i-th element of the classic hysteresis cycle array	T
$RED_{discrete}(x,y)$	Discrete Relative Euclidean Difference between x and y	1
f_s	Sampling frequency	Hz
t_s	Sampling time	s
Statistical variables		
Symbol	**Name**	**Unit**
M_{JS}	Sum of Barkhausen jumps magnetization change	A/m
N	Number of elementary Barkhausen jumps (Eq. 4)	1
$<M_{disc}>$	Average Barkhausen jump magnetization change	A/m
i	Index of the elementary event	1
$\overrightarrow{M_i}$	Magnetization of the i-th elementary cross-surface	A/m
S_i	Cross-surface of the i-th element	m^2
$\overrightarrow{u_i}$	Direction vector for the i-th elementary cross-surface	-
N_d	Number of elementary domains	1
f	Elementary magnetization change function	-
t_c	Commutation time	s
τ	Elementary event demi-duration	s
θ, Φ	Spherical coordinates angles	rad
n_s	Half-length of the elementary peaks (in number of samples)	1
A	Elementary event amplitude (section 3.2)	V
t_R	Elementary event peak time (rising branch, section 3.2)	s
t_F	Elementary event peak time (falling branch, section 3.2)	s
σ	Elementary event time variance (section 3.2)	$s^{0.5}$

p	Probability functions	-
$\overline{\overline{X}}$	Cardinality of the set X	1
$\bar{s}$	Average elementary cross-surface	m^2
μ_D	Mean of distribution D	-
σ_D	Standard deviation of distribution D	-
$\mathcal{N}(\mu;\sigma^2)$	Normal distribution of average μ and variance σ^2	-
$F_{\mathcal{N}}(L,s)$	Folded Normal distribution of location L and scale s	-

1 – Introduction

Magnetic Barkhausen Noise (MBN) is a peculiar manifestation of ferromagnetic materials. It is a fascinating academic topic [1] and a useful industrial tool [2]-[4]. By indirectly reflecting the microstructural properties and the level of residual stress, MBN gives access to essential information. Industrial non-destructive controllers have been developed for the use of MBN as a way to detect grinding burns [5], evaluate case depth [6] and the profile of residual stresses [7][8].

The origin of Barkhausen noise is associated with the kinetic of the magnetic domains during the magnetization process. Ferromagnetism comes from atomic magnetic moments of electronic origin becoming ordered into small regions known as magnetic domains. In an unmagnetized state, each magnetic domain typically comprises 10^{12} to 10^{18} magnetic moments aligned in the same direction and orientation [9]. At the domain boundaries known as domain walls, a change in the direction of the atomic magnetic moment gradually takes place over several hundred atoms whose exact number depends on energetical balance.

The magnetization process in a ferromagnetic part is illustrated in Fig. 1 and supports multiple mechanisms: firstly, the magnetic domains with a magnetization oriented favorably to the applied magnetic field grow, while the domains unfavorably oriented decline in proportion. Then, the magnetization of the resulting domain, initially oriented along an easy axis, coherently rotates toward the direction of the applied magnetic field [9][10].

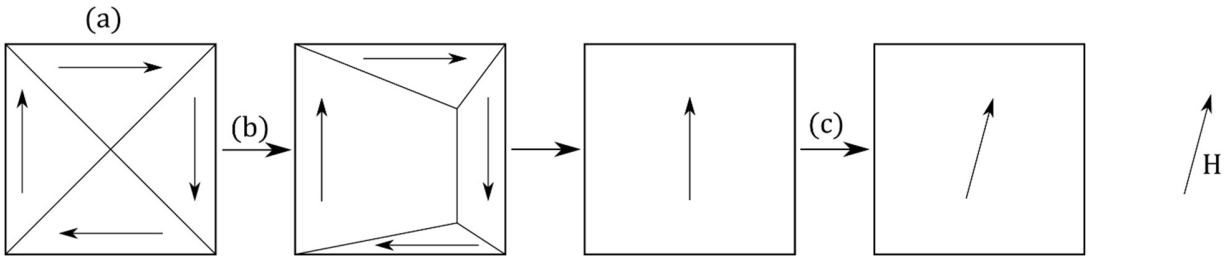

Fig. 1 – Schematic illustration of the magnetization process. (a) Unmagnetized state (b) Domain wall motion (c) Magnetization rotation.

Domains change their size by the domain walls moving within the crystal lattice in response to changes in the magnetic field [11]. Each motion generates a sudden micro-change in magnetization and magnetic flux. In bulk specimens, this process accumulates simultaneous micro-flux variations that eventually get strong enough to be detected by magnetic flux sensors. MBN is the resulting raw signal.

The magnetic domains' kinetic has been proven reproducible for thin film specimens when the overall magnetic state and domain distribution can be controlled [12][13]. It is, however, impossible to force the domain distribution in a bulk specimen. MBN is, in these conditions, considered a stochastic phenomenon, and its analysis has to be done through time-independent indicators. Those include the Root Mean Square (RMS) [14], the $MBN_{envelope}$ [15][16], the sum of peaks during an excitation period [17], or the MBN_{energy} [18][19].

The differential permeability and MBN are highly correlated. Therefore, plotting MBN's time-independent indicators vs. the magnetic tangent surface excitation field H_{surf} always leads to a hysteresis cycle.

In [20], Fagan et al. studied Oriented Grains electrical steel materials (GO FeSi). A strong anisotropy characterized these specimens. Magnetization in the easy direction (RD, Rolling Direction) leads to a limited rotation contribution. For these materials, the $MBN_{energy}(H_{surf})$

hysteresis cycle and the classic $B_a(H_{surf})$ (where B_a is the magnetic flux density) happen to be very similar after a rescaling stage.

In this paper, MBN_{energy} is defined by Eq. 1 with α=2:

$$MBN_{energy}(t) = \int_0^t sign\left(\frac{dH_{surf}}{ds}\right)|V_{MBN}|^{\alpha}(s)ds \quad (1)$$

Where V_{MBN} is the voltage drop along the sensor coil. MBN_{energy} is not an energy per se (its unit is $V^{\alpha}\cdot s^{-1}$), but in [20] and [21], it has been described as proportional to the kinetic energy of domain wall motions. Still, the physical meaning of Eq. (1) is not straightforward, and other definitions of MBN_{energy} have been tested. In [22], Meng et al. justify using $IV_{MBN}I$ (α=1 in Eq. 1) based on theoretical developments picked up in the framework of the Jiles-Atherton model. They demonstrated a proportionality between their definition of MBN_{energy} and M_{irr} (the irreversible magnetization contribution).

This study aims to improve MBN understanding and fully exploit the $MBN_{energy}(H_{surf})$ hysteresis cycles. Our objective is to answer the following questions:

_ How are MBN_{energy} and the magnetization variations correlated?

_ What's the ideal MBN_{energy} definition and renormalization method?

_ Is the magnetization rotation reversible, or do we have associated losses?

_ Is it possible to return the hysteresis property from indirect and surface measurements?

For this, a theoretical study was built to assess both MBN_{energy} definitions from a theoretical point of view. Analytical and numerical results were obtained, and conclusions were drawn. The magnetization rotation was intentionally not considered in this theoretical development, and the focus was limited to the domain wall displacements.

Then, various ferromagnetic steel specimens of different natures were characterized. $B_a(H_{surf})$ and $MBN_{energy}(H_{surf})$ hysteresis cycles were plotted from simultaneous acquisitions of similar sensors and provided experimental confirmations of the theoretical conclusions.

2 – Theoretical consideration

The stochastic nature of the Barkhausen effect has been admitted for decades [23]. It has already been used in the constitutive equations of MBN raw signal simulation tools, like in the ABBM model [24][25]. Similarly, In [26], Jiles et al. described a stochastic model in which the MBN activity M_{JS} is linked to the number of elementary Barkhausen jumps N and their average amplitude M_{disc}:

$$M_{JS} = N < M_{disc} > \tag{2}$$

$$MBN(t) \propto \frac{dM_{JS}}{dt} \tag{3}$$

Unfortunately, these methods have never been extended to the MBN_{energy} simulation and the associated hysteresis loops. In light of this, we proposed in the second part of this study to develop our own simulation tool and check on the theoretical viability of both MBN_{energy} definitions by comparing them to the magnetic flux density.

2.1 – Theoretical framework

Let us consider a specimen of cross-surface S and normal axis $\overrightarrow{e_z}$. The specimen is wrapped by a coil acting as a magnetic flux sensor. S is divided into many elementary volumes N_d, possibly assimilated into a group of domains. Each elementary volume is supposed to be characterized by

an average magnetization $\overrightarrow{M_i}$, and a cross-sectional area S_i. Fig. 2 illustrates the simulation context.

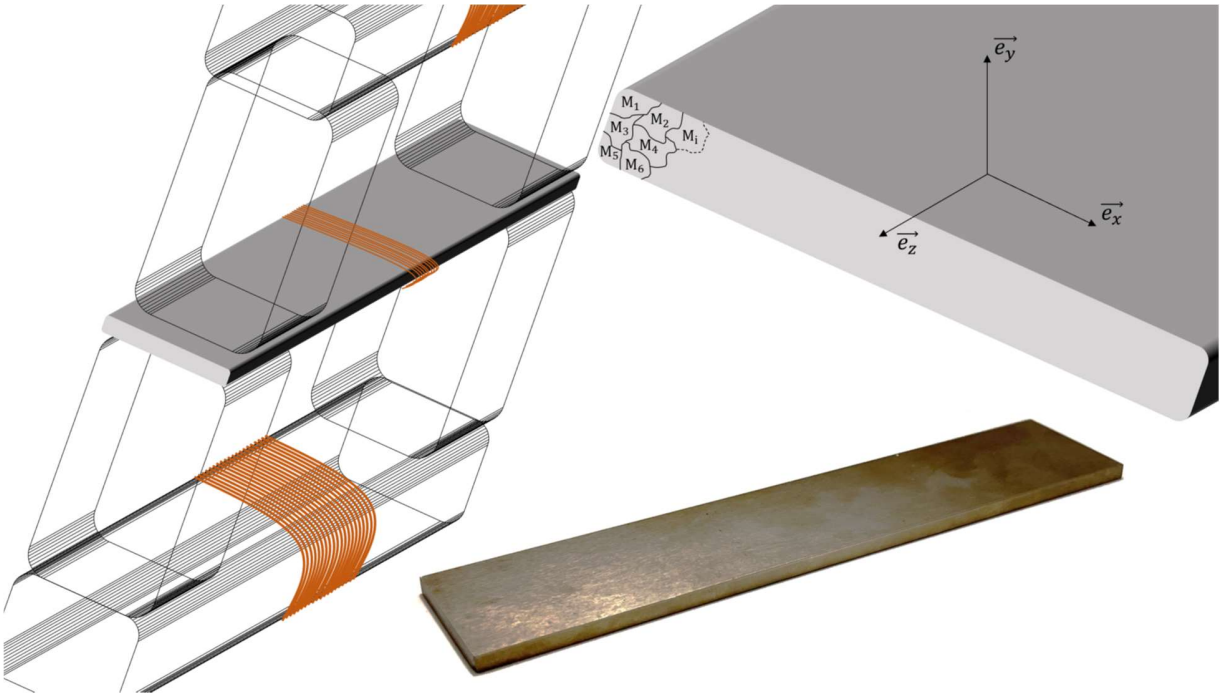

Fig. 2 – Subdivision of the cross-surface in N_d elementary volumes.

The average magnetization variation $\frac{dB_a}{dt}$ can be written as the superposition of the magnetization change in every elementary volume:

$$\frac{dB_a}{dt}(t) = \iint_S \frac{d\vec{B}}{dt} \cdot \overrightarrow{e_z}\, dS = \mu_0 \iint_S \frac{d\vec{H}}{dt} \cdot \overrightarrow{e_z}\, dS + \mu_0 \iint_S \frac{d\vec{M}}{dt} \cdot \overrightarrow{e_z}\, dS \approx \mu_0 \iint_S \frac{d\vec{M}}{dt} \cdot \overrightarrow{e_z}\, dS \quad (4)$$

$$\iint_S \frac{d\vec{M}}{dt} \cdot \overrightarrow{e_z}\, dS = \sum_{i=1}^{N_d} \iint_{S_i} \frac{d\vec{M}}{dt} \cdot \overrightarrow{e_z}\, dS = \sum_{i=1}^{N_d} S_i \frac{d\overrightarrow{M_i}}{dt} \cdot \overrightarrow{e_z} \quad (5)$$

$$\Rightarrow \frac{dB_a}{dt}(t) \approx \mu_0 \sum_{i=1}^{N_d} S_i \frac{d\overrightarrow{M_i}}{dt} \cdot \overrightarrow{e_z} \quad (6)$$

In the following, we consider $\mu_0 \iint_S \frac{d\vec{H}}{dt} \cdot \overrightarrow{e_z}\, dS$ negligible, and we assume a magnetization trajectory starting from a saturated state ($M = -M_{sat}$) and finishing at the opposite saturation state ($M = M_{sat}$). H_{surf} is supposed to be varying at a constant rate:

$$\overrightarrow{H_{surf}}(t) = H_{sat} \cdot (2t-1)\overrightarrow{e_z}; t \in [0;1] \quad (7)$$

$$\forall i \in [1;N] \begin{cases} \overrightarrow{M_i}(0) = -M_{sat}\overrightarrow{e_z} \\ \overrightarrow{M_i}(1) = M_{sat}\overrightarrow{e_z} \end{cases} \quad (8)$$

The elementary magnetization change $\frac{\mathrm{dM_i}}{\mathrm{dt}}$ is supposed to be derived from a unique function f. Each change is characterized by its peak time t_{c_i}, and spread time τ_i. f is defined by Eq. 9 and must comply with conditions Eq. 10:

$$\frac{dM_i}{dt}(t) = f\left(\frac{t-t_{c_i}}{\tau_i}\right) \quad (9)$$

$$\begin{gathered} f(x) \geq 0 \; \forall x \in \mathbb{R} \\ max(f) = f(0) = 1 \\ f(|x| \geq 1) = 0 \end{gathered} \quad (10)$$

A large variety of envelopes can be obtained from Eq. 9 and 10. In Fig. 3, a rectangular function, a Gaussian envelope, and an asymmetrical function are plotted as examples.

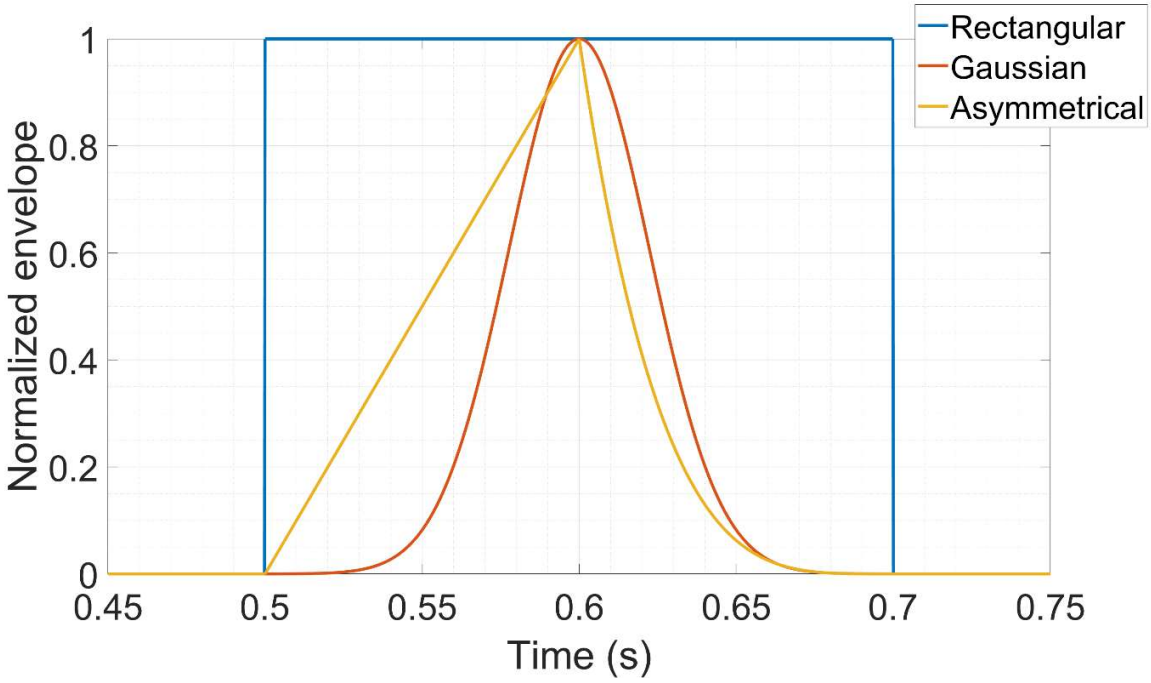

Fig. 3 – f illustration, for $t_c = 0.6$ and $\tau = 0.1$.

The next step of the simulation process relies on the experimental observations depicted in Fig. 4. Here, a set magnetic yoke/excitation coil magnetized a ferromagnetic sheet crossed by a n = 25 turns search coil. A relatively homogeneous Barkhausen noise signal is observed for different magnetization angles. The signal amplitude is slightly lower when the sensor is aligned with the magnetic excitation, but these minor variations can be credited to the holes drilled, partially shielding the magnetic field (This issue has already been discussed in [27]). Oppositely, the signal at the magnetization frequency shows significant differences vs. the magnetization angle. It even entirely disappears when the coil senses no magnetization variation (right bottom part of Fig. 4).

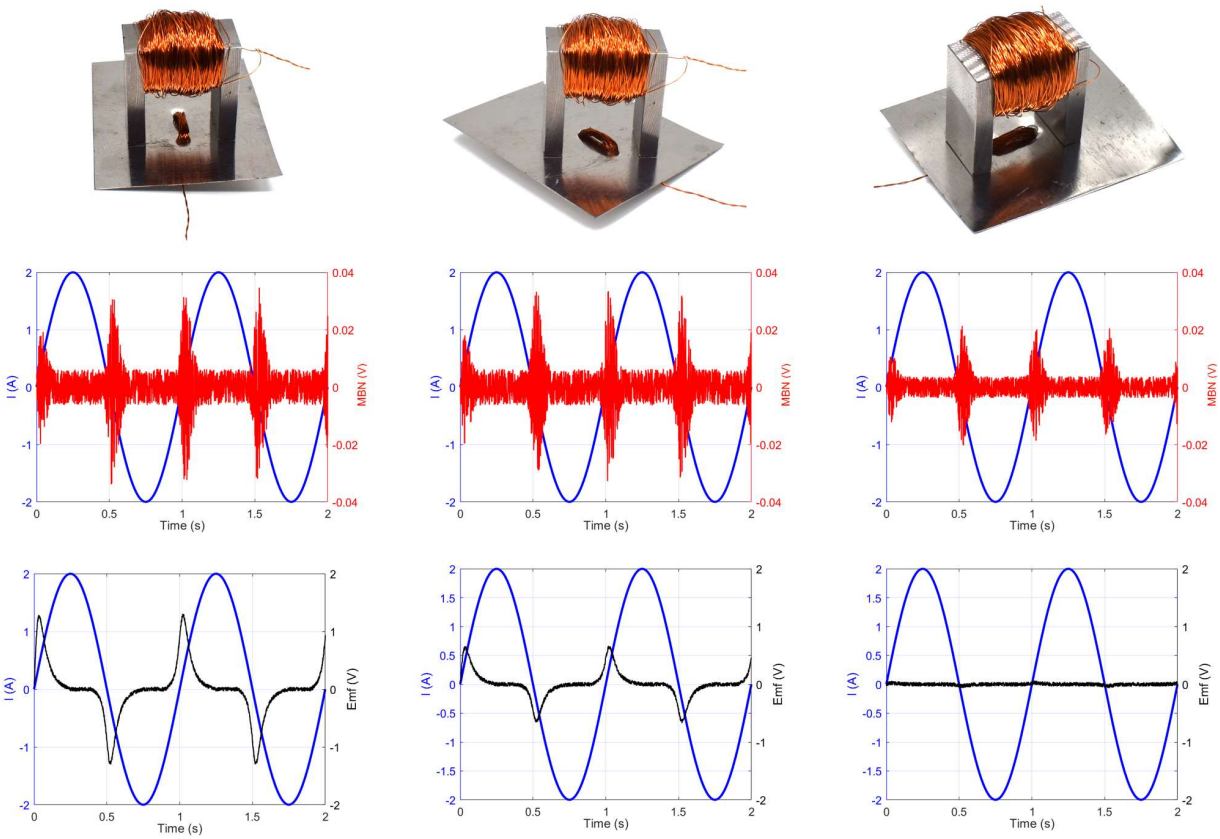

Fig. 4 – Magnetic flux variations and MBN raw signal for different orientations of the sensor coil.

Based on these experimental observations, we propose two contributions associated with the elementary magnetization changes:

- A « normal » magnetization change, aligned with the external magnetic field and which can be related to the temporal variation of the magnetic flux density $B_a(t)$:

$$\frac{dB_a}{dt}(t) = \mu_0 \sum_{i=1}^{N_d} S_i \frac{dM_i \overrightarrow{e_z}}{dt} \cdot \overrightarrow{e_z} = \mu_0 \sum_{i=1}^{N_d} S_i \frac{dM_i}{dt} \quad (11)$$

(It is worth reminding the absence of the magnetization rotation contribution in this theoretical expression of the magnetic flux density).

- A stochastic magnetization change, whose direction is random and which can be associated with the magnetic Barkhausen noise raw signal. A domain wall is supposed to contain all 2D magnetization directions and can move in all directions. Isotropic magnetic behavior is considered in Eq. 12):

$$V_{MBN}(t) = \mu_0 \sum_{i=1}^{N_d} S_i \frac{dM_i \begin{pmatrix} cos\theta_i\, cos\phi_i \\ sin\theta_i\, cos\phi_i \\ sin\,\phi_i \end{pmatrix}}{dt} \cdot \overrightarrow{e_z} = \mu_0 \sum_{i=1}^{N_d} S_i sin\phi_i \frac{dM_i}{dt} \quad (12)$$

$$\theta_i = 2\pi\, R_{1_i};\ \phi_i = asin\,(2R_{2_i} - 1) \quad (13)$$

Here, θ and ϕ are the angles in a spherical coordinates system, R_1 and R_2 two random uniform distributions of extrema 0 and 1. V_{MBN} stands for the voltage drop along the sensor coil aligned with the lamination width, as illustrated in Fig. 2. dB_a/dt and V_{MBN} (Eq. 11 and 12) are obtained from Fig. 5 model based on the Probability Distribution Functions (PDF) ruling parameters τ and t_c.

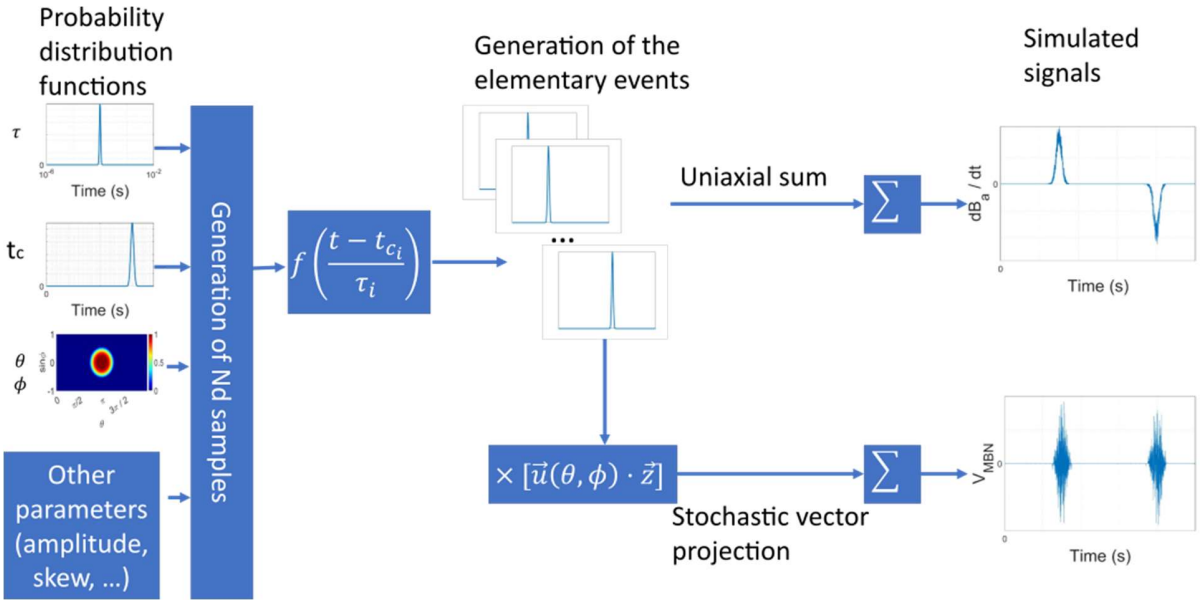

Fig. 5 – Flow diagram of the simulation procedure.

After integration, Eq. 11 and 12 give, respectively, the simulated flux density B_a (Eq. 14) and the simulated MBN_{energy} (Eq. 15):

$$B_a(t) = \mu_0 \int_0^t \sum_{i=1}^{N} S_i \frac{dM_i}{ds}\, ds \tag{14}$$

$$MBN_{energy}(t) = \int_0^t sign\left(\frac{dH}{ds}\right) |V_{MBN}|^{\alpha}(s) ds \tag{15}$$

In this approach, B_a variations are entirely due to discrete magnetization variations. The rotation contribution is not considered. Since our objective is to compare the $B_a(H_{surf})$ and the $MBN_{energy}(H_{surf})$ cycles under the unique influence of the domain wall motions, the absence of rotation is not detrimental.

In the following, all simulation tests were limited to α = 1 [22] and α = 2 [16][18][20], but a positive fractional value can be considered as well.

2.2 – Analytical developments

2.2.1 – Short time magnetization variation: small τ_i

Let us consider small τ_i cases first. Such a condition is plausible considering the fast dynamics of domain wall motions (in the sub-microsecond scale [28]). The set of active events at t is called X and is defined by Eq. 16:

$$X(t) = \left\{ i \in [\![1; N_d]\!] \mid \frac{dM_i}{dt}(t) > 0 \right\} \tag{16}$$

which implies, thanks to Eq. 10, that:

$$X(t) = \left\{ i \in [\![1; N_d]\!] \mid f\left(\frac{t - t_{c_i}}{\tau_i}\right) > 0 \right\} = \left\{ i \in [\![1; N_d]\!] \mid \left|t - t_{c_i}\right| < \tau \right\} \tag{17}$$

The time variation of the flux density is reduced to the active events contribution:

$$\frac{dB_a}{dt}(t) = \frac{\mu_0 \sum_{i=1}^{N_d} S_i \frac{dM_i}{dt}(t)}{S} = \mu_0 \frac{\sum_{i \in X(t)} S_i \frac{dM_i}{dt}(t)}{S} \tag{18}$$

The number of elements of the set X is called cardinality and is noted $\overline{\overline{X}}$ in this paper. If N_d is large enough, $\overline{\overline{X}}$ can be approximated by Eq. 19:

$$\overline{\overline{X}}(t) = card\big(X(t)\big) \approx N_d \int_{t-\tau}^{t+\tau} p(t_c = s) ds \tag{19}$$

When $\tau_i \to 0$ and $S_i = \bar{s} + \Delta S_i \approx \bar{s}$ (where $\bar{s} = S/N_d$ is the average of the elementary volumes' cross-section), only elementary events for which $t_{c_i} = t$ are non-zero. This case can be approached by taking rectangular windows and a sampling frequency $f_s = \frac{1}{2\tau}$. In this case, an elementary event can be represented by a discrete Dirac function $\delta(t - t_{c_i})$, and it is illustrated in Fig. 6.

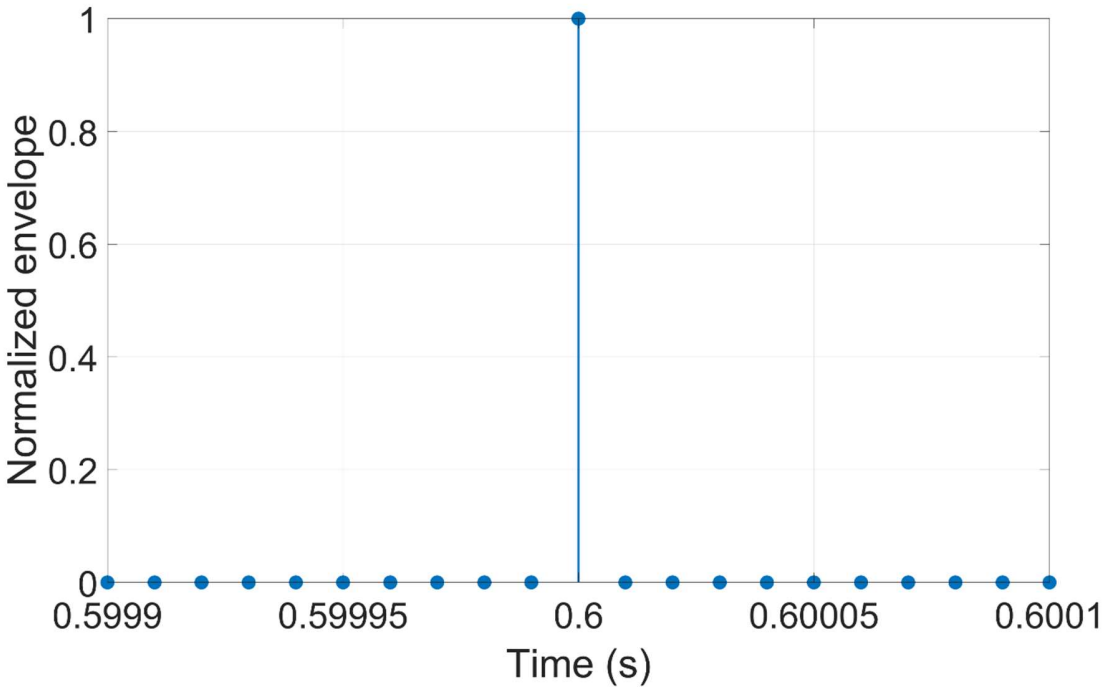

Fig. 6 – Elementary function f for small τ (t_c = 0.6).

In such condition, Eq. 19 can be simplified as follows:

$$\frac{dB_a}{dt}(t) \approx \mu_0 \frac{\bar{s} \sum_{i \in X(t)} f(0)}{S} \tag{20}$$

$$\frac{dB_a}{dt}(t) \approx \mu_0 \frac{\bar{\bar{X}}(t)}{N_d} \tag{21}$$

The flux density variation becomes directly proportional to the peak times probability distribution. The random angle makes applying the same process to the MBN signal (Eq. 12) less straightforward:

$$V_{MBN}(t) \approx \frac{\mu_0}{N_d} \sum_{i \in X(t)} sin\phi_i \cdot f(O) \tag{22}$$

A complete development of Eq. 22 is available in Annex 1, but a straightforward and pragmatic approach consists of squaring both terms in Eq. 22:

$$V_{MBN}^2(t) \approx \frac{\mu_0^2}{N_d^2} \left(\sum_{i \in X(t)} sin\phi_i \right)^2 \tag{23}$$

$$V_{MBN}^2(t) \approx \frac{\mu_0^2}{N_d^2}\left(\sum_{i\in X(t)} sin^2\,\phi_i \; + 2\,\sum_{i\in X(t)}\sum_{\substack{j\in X(t)\\ j>i}} sin\,\phi_i\, sin\,\phi_j\right) \quad (24)$$

$$V_{MBN}^2(t) \approx \frac{\mu_0^2}{N_d^2}\left[\sum_{i\in X(t)}\frac{1}{2}(1-cos\,2\phi_i) \; + 2\,\sum_{i\in X(t)}\sum_{\substack{j\in X(t)\\ j>i}} sin\,\phi_i\, sin\,\phi_j\right] \quad (25)$$

$$V_{MBN}^2(t) \approx \frac{\mu_0^2}{N_d^2}\left[\frac{1}{2}\bar{\bar{X}}(t) - \frac{1}{2}\sum_{i\in X(t)} cos\,2\phi_i \; + 2\,\sum_{i\in X(t)}\sum_{\substack{j\in X(t)\\ j>i}} sin\,\phi_i\, sin\,\phi_j\right] \quad (26)$$

The resulting V_{MBN}^2 signal depends on the number of events and two random sums. Since all angles are derived from the same probability distribution, the Central Limit Theorem (CLT) can be applied: as long as the number of elements N is significant, the normalized distribution D_N derived from a distribution D of average μ_D and variance σ_D^2 converges towards a normal law $\mathcal{N}(0;\,\sigma_D^2)$ of mean 0 and variance σ_D^2 (Eq. 27):

$$\begin{cases} D_N = \frac{\sum_{k=1}^{N} D_k}{N} \\ \sqrt{N}\,(D_N - \,\mu_D) \xrightarrow[N\to+\infty]{} \mathcal{N}(0;\,\sigma_D^2) \end{cases} \quad (27)$$

$\bar{\bar{X}}(t)$ has to be large enough to satisfy the CLT hypothesis.

The two random distributions in Eq. 26 are noted A and B in the next equations, and their averages μ_A and μ_B:

$$A = \sum_{i\in X(t)} cos\,2\phi_i \approx \mu_A\bar{\bar{X}}(t) \Rightarrow \mu_A = \frac{\sum_{i\in X(t)} cos\,2\phi_i}{\bar{\bar{X}}(t)} \quad (28)$$

$$B = \sum_{i\in X(t)}\sum_{\substack{j\in X(t)\\ j>i}} sin\,\phi_i\, sin\,\phi_j \approx \mu_B\bar{\bar{X}}(t)\frac{\bar{\bar{X}}(t)-1}{2} \Rightarrow \mu_B = \frac{\sum_{i\in X(t)}\sum_{\substack{j\in X(t)\\ j>i}} sin\,\phi_i\, sin\,\phi_j}{\bar{\bar{X}}(t)\frac{\bar{\bar{X}}(t)-1}{2}} \quad (29)$$

Using μ_A and μ_B, Eq. 26 becomes:

$$V_{MBN}^2(t) \approx \frac{\mu_0^2}{N_d^2}\left[\frac{1}{2}\bar{\bar{X}}(t) - \frac{1}{2}\bar{\bar{X}}(t)\mu_A \; + 2\;\bar{\bar{X}}(t)\frac{\bar{\bar{X}}(t)-1}{2}\,\mu_B\right] \quad (30)$$

$$V_{MBN}^2(t) \approx \frac{\mu_0^2}{N_d^2}\left\{\bar{\bar{X}}(t)\left[\frac{1}{2} - \frac{1}{2}\mu_A - \mu_B\right] + \;\bar{\bar{X}}(t)^2\,\mu_B\right\} \quad (31)$$

$$V_{MBN}^2(t) \approx \frac{\mu_0^2}{2\,N_d^2}[1-\mu_A-2\mu_B]\,\bar{\bar{X}}(t) + \frac{\mu_0^2}{N_d^2}\,\mu_B\bar{\bar{X}}(t)^2 \quad (32)$$

$$V_{MBN}^2(t) \approx a\left|\frac{dB_a}{dt}\right| + b\left(\frac{dB_a}{dt}\right)^2 \quad (33)$$

$$\begin{cases} a = \dfrac{\mu_0^2}{2N_d^2}[1-\mu_A-2\mu_B] \\ b = \dfrac{\mu_0^2}{N_d^2}\mu_B \end{cases}$$

Finally, V_{MBN}^2 turns into a linear combination of $\left|\frac{dB_a}{dt}\right|$ and $\left(\frac{dB_a}{dt}\right)^2$.

Since μ_A and μ_B depend on ϕ, a and b calculus are not easily generalized, but numerical simulations can be run (see next section), and analytical results can be calculated for specific conditions. Those includes:

- $\mu_B = 0$: $V_{MBN}^2(t) \propto \frac{dB_a}{dt}(t)$, regardless of the value of μ_A. This case leads to a good approximation of B_a by $MBN_{energy\ \alpha=2}$.
- All elementary magnetization variations are in the same direction ϕ: $\mu_A = \cos 2\phi$ and $\mu_B = \sin^2\phi$. Hence, a and b become:

$$b = \frac{\mu_0^2}{N_d^2}\,sin^2\phi \quad (34)$$

$$a = \frac{\mu_0^2}{2\,N_d^2}[1-cos\,2\phi-2\,sin^2\phi] = 0 \quad (35)$$

In this case, V_{MBN}^2 is proportional to B_a, and $MBN_{energy\ \alpha=1}$ gives a better approximation.

- Isotropic distribution of the magnetization variations angle: a and b can be calculated analytically through the Law of the Unconscious Statistician (LOTUS) theorem [29] (see Annex. 2 for details). In this case, Eq. 26 becomes:

$$V_{MBN}^2(t) \approx \bar{s}^2\left[\frac{1}{2}\bar{\bar{X}}(t) - \frac{1}{2}\bar{\bar{X}}(t)\mu_A + 2\,\bar{\bar{X}}(t)\frac{\bar{\bar{X}}(t)-1}{2}\,\mu_B\right] \quad (36)$$

$$V_{MBN}^2(t) \approx \bar{s}^2 \left[\frac{1}{2}\bar{\bar{X}}(t) - \frac{1}{6}\bar{\bar{X}}(t)\right] \quad (37)$$

$$V_{MBN}^2(t) \approx \frac{\bar{s}^2}{3}\bar{\bar{X}}(t) \quad (38)$$

$$V_{MBN}^2(t) \propto \left|\frac{dB_a}{dt}\right|(t) \quad (39)$$

Under an isotropic distribution of random angles ϕ, V_{MBN}^2 becomes proportional to the time variation of the flux density. In these conditions, $MBN_{energy\ \alpha=2}$ becomes proportional to B_a (Eq. 40):

$$V_{MBN}^2(t) \propto \frac{dB_a}{dt}(t) \Rightarrow \int_0^t V_{MBN}^2(s)ds \propto \int_0^t \left|\frac{dB_a}{ds}\right|(s)ds$$

$$\Rightarrow \int_0^t sign\left(\frac{dH_{surf}}{ds}\right) V_{MBN}^2(s)ds \propto \int_0^t sign\left(\frac{dH_{surf}}{ds}\right)\left|\frac{dB_a}{ds}\right|(s)ds$$

$$\Rightarrow MBN_{energy\ \alpha=2}(t) \propto B_a(t) \quad (40)$$

Φ_i has a random distribution and is not regularly spaced from $-\frac{\pi}{2}$ to $\frac{\pi}{2}$. Therefore, the sum is not null, even in the isotropic case. This result is not intuitive, considering that $\int_{-\frac{\pi}{2}}^{\frac{\pi}{2}} sin\theta d\theta = 0$.

2.2.2 – Long time magnetization change: large τ_i

The discrete Dirac function has been used in the previous section to approximate elementary events. Analytical solutions were obtained. Still, experimental observations of magnetization variations associated with the Barkhausen effect on the millisecond scale have also been reported [30]. Therefore, a more general case of non-Dirac function is studied in this sub-section to comply with these slower displacements.

For simplicity, an event is considered by a peak with two successive non-zero elements:

$$t \neq \{0; t_s\} \rightarrow f(t) = 0 \quad (41)$$

Where t_s is the sampling time. For example, Fig. 7 depicts five different peaks (defined by their t_c), and the resulting sum signal.

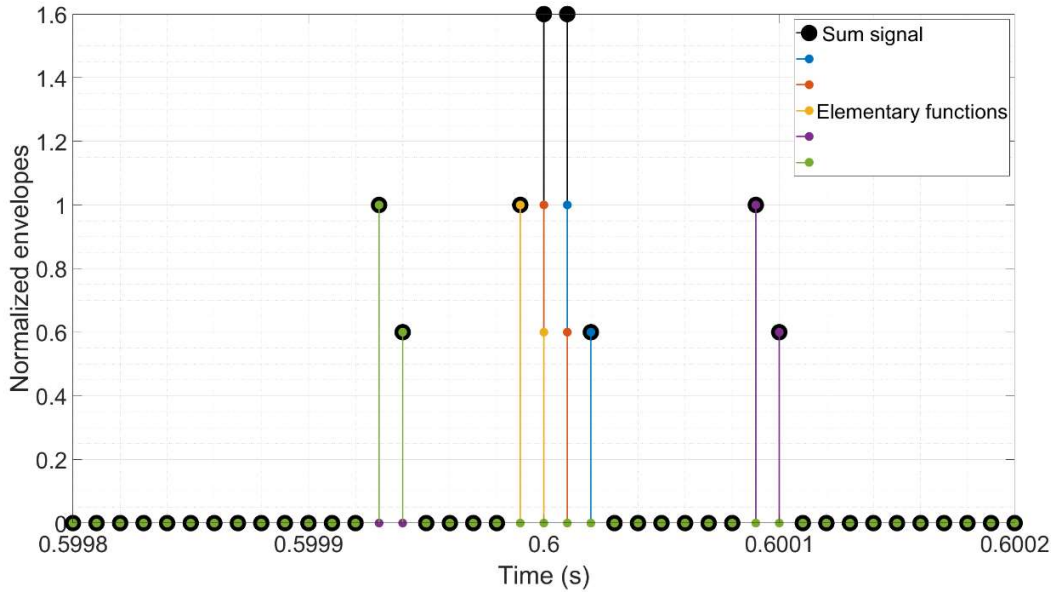

Fig. 7 – Elementary function f when $\tau_i \neq 0$. Five different envelopes are shown in addition to the sum signal.

In these conditions, Eq. 20, 21, and 22 are modified as follows:

$$\frac{dB_a}{dt}(t) = \sum_{i=1}^{N} f\left(t - t_{c_i}\right) \tag{42}$$

$$\frac{dB_a}{dt}(t) = f(0)\ \sum_{i\in X(t)} 1 + f(t_s) \sum_{i\in X(t-t_s)} 1 \tag{43}$$

$$\frac{dB_a}{dt}(t) = f(0)\bar{\bar{X}}(t) + f(t_s)\bar{\bar{X}}(t - t_s) \tag{44}$$

$$V_{MBN}(t) \approx\ f(0) \sum_{i\in X(t)} sin\phi_i + f(t_s) \sum_{i\in X(t-t_s)} sin\phi_i \tag{45}$$

$$V_{MBN}^2(t) =\ f(0)^2\left(\sum_{i\in X(t)} sin\phi_i\right)^2 + f(t_s)^2\left(\sum_{i\in X(t-t_s)} sin\phi_i\right)^2 + 2f(0)f(t_s)\left[\sum_{i\in X(t)} sin\phi_i\right]\left[\sum_{j\in X(t-t_s)} sin\phi_j\right] \tag{46}$$

Eq. 46 is not developed for the sake of brevity. When ϕ_i distribution is homogeneous, V_{MBN}^2 can be written as:

$$V_{MBN}^2(t) \approx \frac{1}{3}\, f(0)^2 \bar{\bar{X}}(t) + \frac{1}{3} f(t_s)^2 \bar{\bar{X}}(t - t_s) \tag{47}$$

V_{MBN}^2 becomes proportional to $|dB_a/dt|$ when $\bar{\bar{X}}(t)$ and $\bar{\bar{X}}(t - t_s)$ are identical. If the peak length is negligible compared to the time evolution of $\frac{dB_a}{dt}$, $\bar{\bar{X}}(t)$ can be considered constant for the duration of the elementary peaks. Hence, if one considers elementary peaks with a duration of $2n_s$-1 samples, then:

$$\bar{\bar{X}}(t + k\ t_s) \approx \bar{\bar{X}}_{avg}\ \forall k \in [\![-n; n]\!] \tag{48}$$

$$\left|\frac{dB_a}{dt}\right|(t) = \sum_{k=-n_s}^{n_s} \bar{\bar{X}}(t - k\ t_s) f(k\ t_s) \tag{49}$$

$$\left|\frac{dB_a}{dt}\right|(t) \approx \bar{\bar{X}}_{avg} \sum_{k=-n_s}^{n_s} f(k\ t_s) \tag{50}$$

$$V_{MBN}^2(t) \approx \frac{1}{3} \sum_{k=-n_s}^{n_s} \bar{\bar{X}}(t - k\ t_s) f(k\ t_s)^2 \tag{51}$$

$$V_{MBN}^2(t) \approx \frac{1}{3} \bar{\bar{X}}_{avg} \sum_{k=-n_s}^{n_s} f(k\ t_s)^2 \tag{52}$$

Such equations could be valid approximations for “small” elementary events or low-frequency dynamics (equivalent to quasi-static excitation fields). Still, it would not fill the CLT requirement to have a significant number of events. These results make it complex to conclude with the comparison between the $B_a(H_{surf})$ and the $MBN_{energy}(H_{surf})$ hysteresis cycles.

2.3 – Numerical simulations

2.3.1 – Short time magnetization change: small τ_i

In this sub-section, the simulation conditions are those of section 3.2.1 (Eq. 21 and 22), and the parameters’ values are given in Table 1:

Parameter	Value
f_s	1 MHz
N_d	$3 \cdot 10^5$
$p(t_c = t)$	$\frac{1}{0.08\sqrt{\pi}} e^{-\left(\frac{t-0.3}{0.08}\right)^2}$
Angle distribution for V_{MBN}	Isotropic

Tab. 1 – Numerical simulation parameters.

Normalized MBN_{energy} and B_a and superposed in Fig. 8. Their respective REDs (Relative Euclidean Difference) are plotted vs. the number of events in Fig. 9.

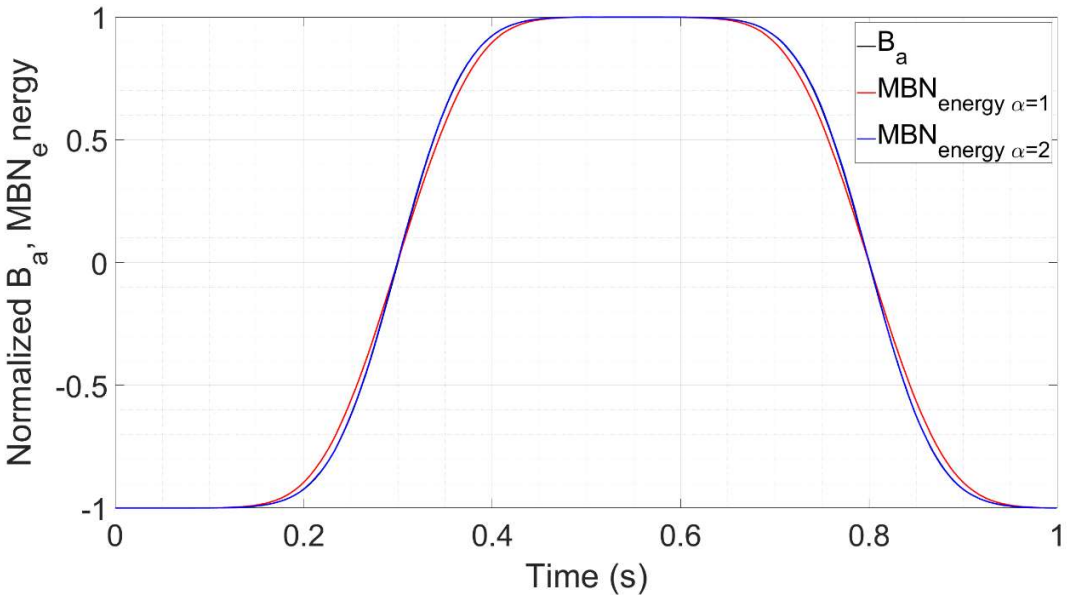

Fig. 8 – Time variations of normalized $MBN_{energy\ \alpha=1}$, $MBN_{energy\ \alpha=2}$, and B_a.

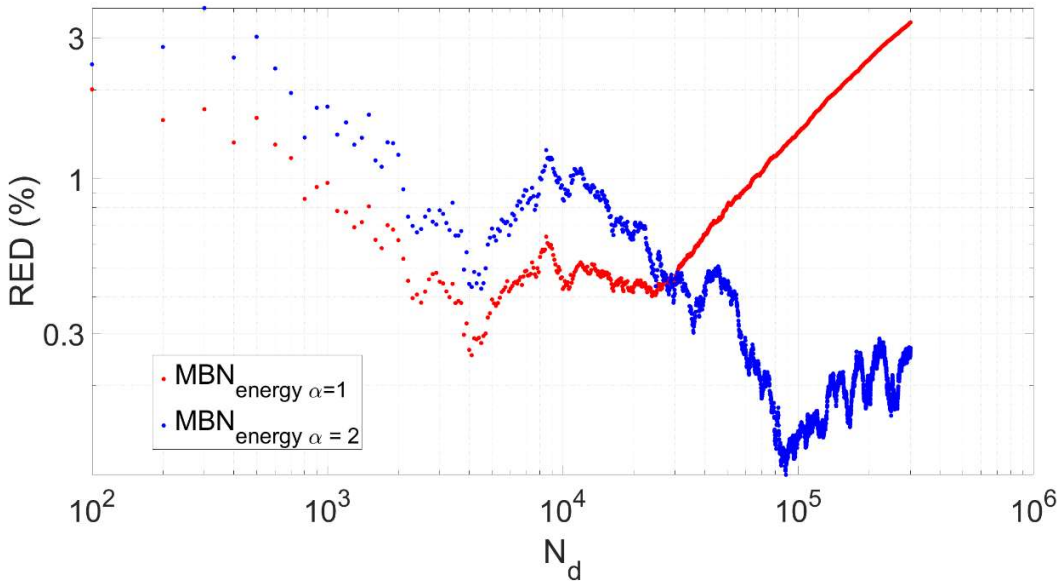

Fig. 9 – Comparison $MBN_{energy\ \alpha=1}$ and $MBN_{energy\ \alpha=2}$ RED vs. the number of events.

Once N_d becomes large enough (> $2 \cdot 10^4$ in Fig. 9), $MBN_{energy\ \alpha=2}(H_{surf})$ becomes a better approximation. The exact number of events depends on the ratio between the average peak width τ and the "time spread" (the length of time in which elementary events take place, in this example, proportional to 0.08).

2.3.2 – Long time magnetization change: large τ_i

In this sub-section, we extend 3.3.1 numerical results to more realistic cases (complex to be solved analytically). Here $N_d = 10^5$, f_s = 100 kHz, and a combination of two Gaussian envelopes is considered as the elementary peak function:

$$\frac{dM_i}{dt}(t) = A_i \left[e^{-\frac{\left(t-t_{R_i}\right)^2}{2\sigma_i^2}} - e^{-\frac{\left(t-t_{F_i}\right)^2}{2\sigma_i^2}} \right] \tag{53}$$

Fig. 10 illustrates large τ_i cases with a sum of five elementary functions defined by Eq. 53. One can notice the resulting signal's distorted shape due to the elementary functions' superposition.

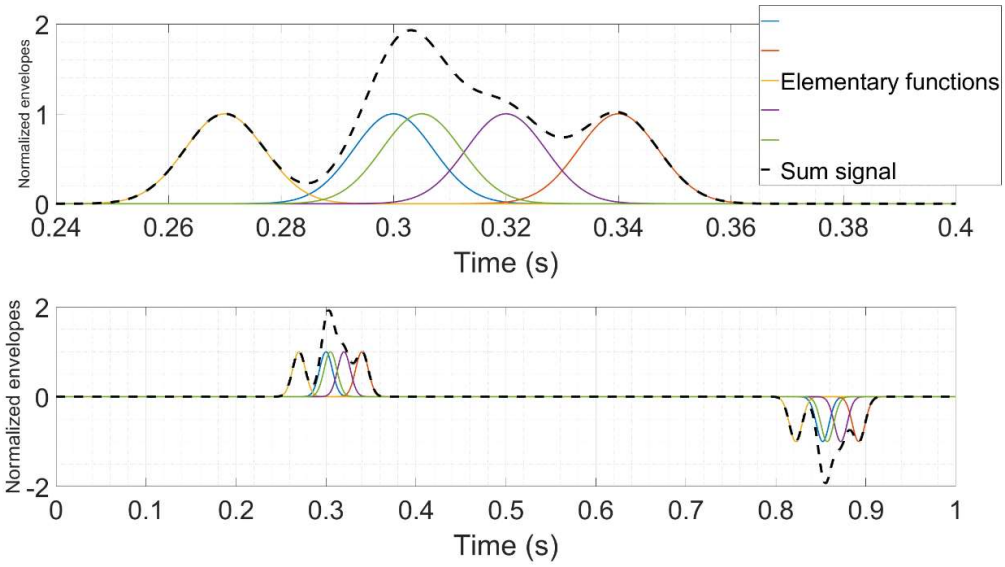

Fig. 10 – Elementary functions and resulting signal.

Eq. 53 is characterized by four parameters (amplitude A, time spread σ, positions of the rising peak t_R, and position of the falling peak t_F). Every parameter is ruled by a normal law, besides σ, in which its logarithm follows a normal law. The parameter's mean and variance are listed in Table 2 below:

	Mean	Variance
$\mathbf{A}$	1	0.1
$\mathbf{t_R}$	0.3	0.05
$\mathbf{t_F}$	0.8	0.05
$\mathbf{\log_{10}\sigma}$	-4	0.1

Tab. 2 – Mean and variance of each simulation parameter.

The influence of A is null as the simulation results are renormalized on the Y-axis (Induction axis). All other parameters have been set to obtain simulation results coherent with the experimental observations (with a simulated triangular H_{surf} field of amplitude H_{sat} and frequency

1 Hz). ϕ is supposed to follow Eq. 13. Simulation results are shown in Fig. 11 and Fig. 12 below. In such a configuration, the $MBN_{energy\ \alpha=2}(H_{surf})$ cycle coincides perfectly with the $B_a(H_{surf})$'s one. Oppositely, the comparison with the $MBN_{energy\ \alpha=1}(H_{surf})$ cycle depicts much more significant differences.

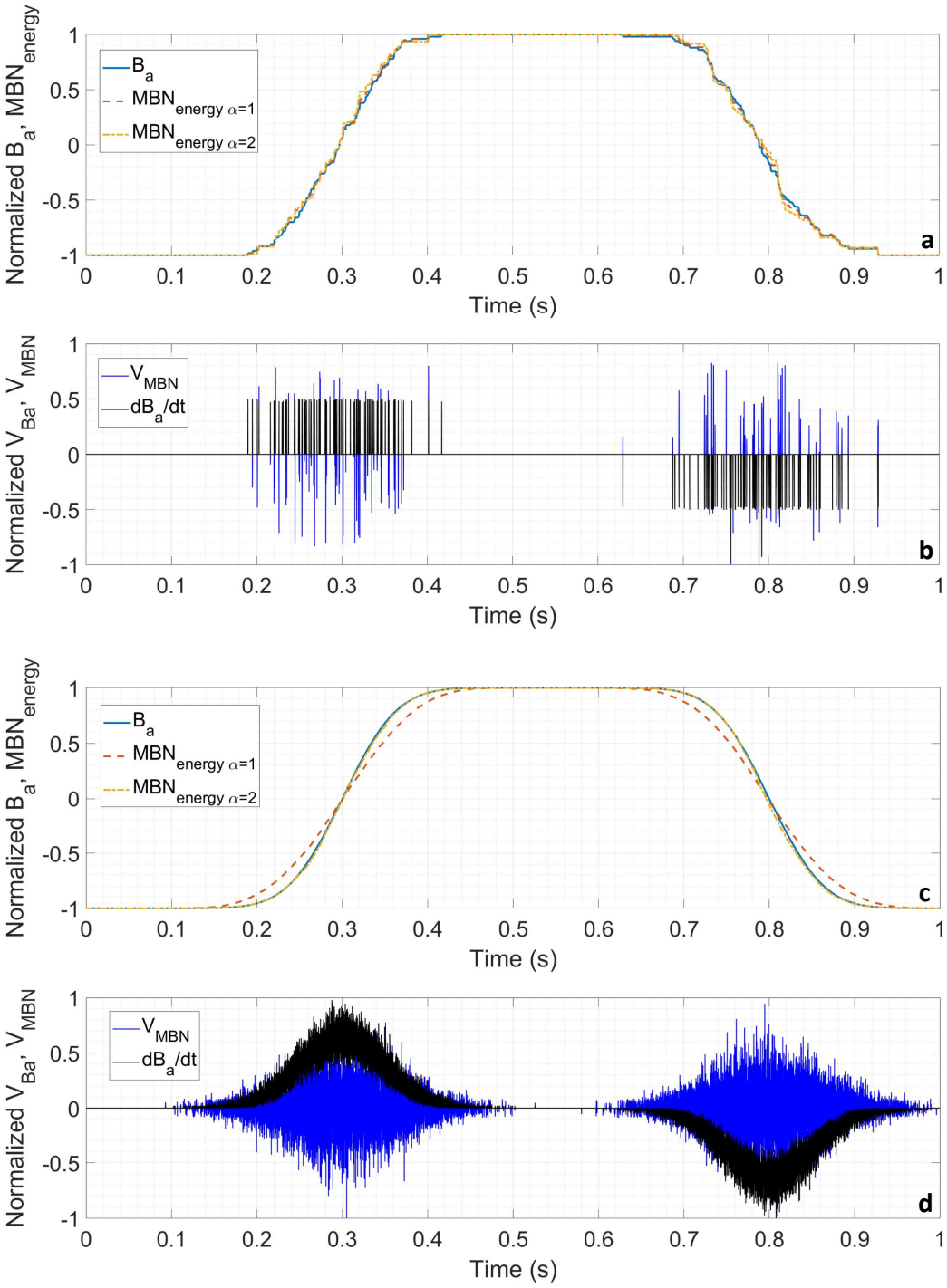

Fig. 11 – a, c Comparison simulated B_a and MBN_{energy} time signals after renormalization (a: $N_d = 100$, c: $N_d = 10^5$). Fig. 11 – b, d MBN and dB_a/dt raw signal vs. time (b: $N_d = 100$, d: $N_d = 10^5$).

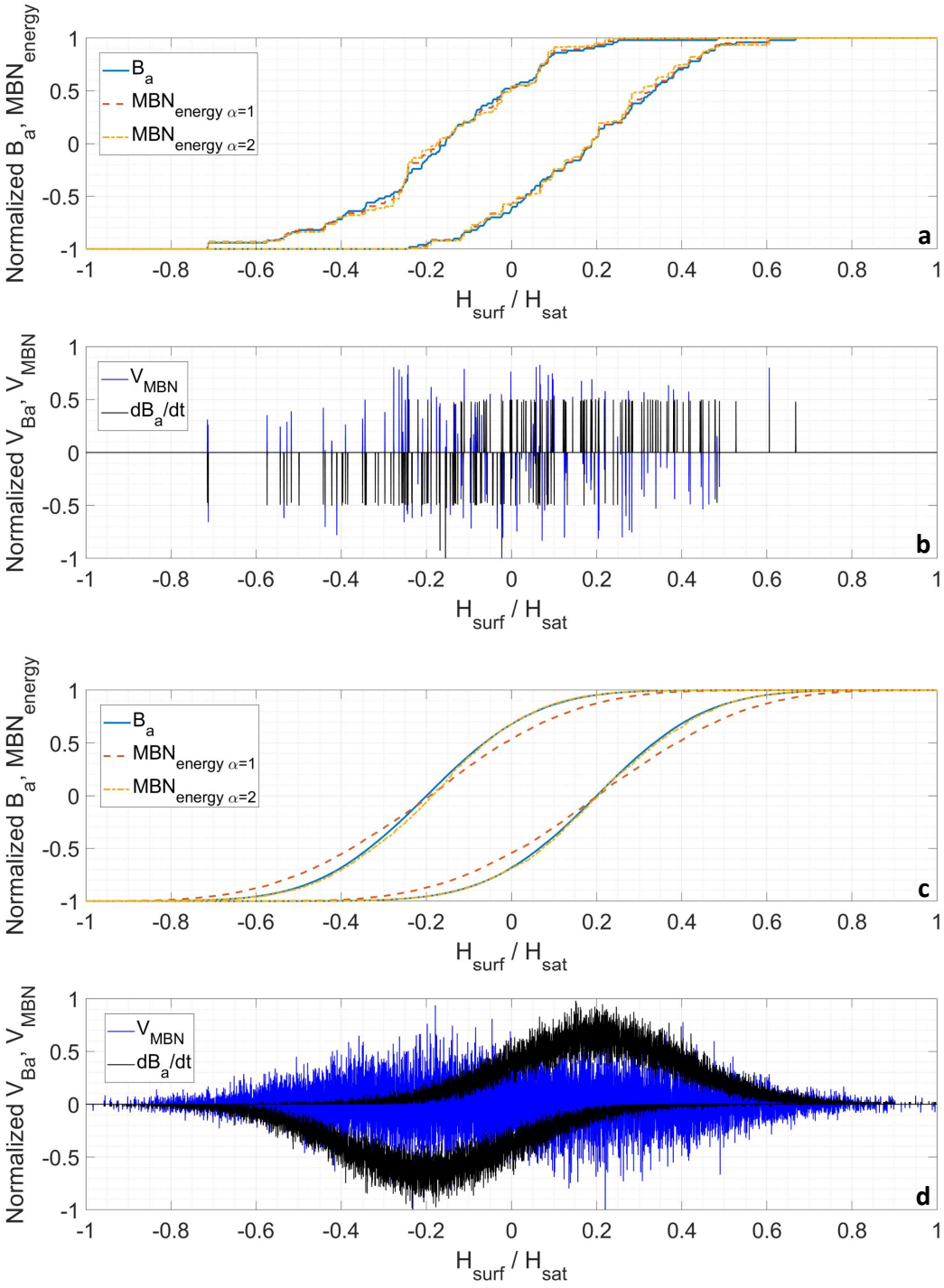

Fig. 12 – a, c Comparison simulated B_a and MBN_{energy} hysteresis cycles after renormalization (a: N_d = 100, c: $N_d = 10^5$). Fig. 12 – b, d MBN and dB_a/dt raw signal vs. H_{surf} (b: N_d = 100, d: $N_d = 10^5$).

As illustrated in Fig. 11 and Fig. 12, the simulation results highly depend on the number of elementary events N_d. Fig. 13 shows a significant influence of the time variance t_R and t_F. This dependency was also noticed in the analytical analysis. A good approximation of the $B_a(H_{surf})$ by the $MBN_{energy}(H_{surf})$ is only obtained with a large number of events. If the variance of both t_R and t_F is weak (in other words, if the hysteresis loop is very stiff) $B_a(H_{surf})$ and $MBN_{energy\ \alpha=1}$ look similar. However, if the Barkhausen activity is spread on a wide interval (high time variance), then $MBN_{energy\ \alpha=2}$ gives a much better approximation of $B_a(H_{surf})$. For an excitation frequency of 1 Hz, the experimental observations commonly show time variances in the order of 0.1 s.

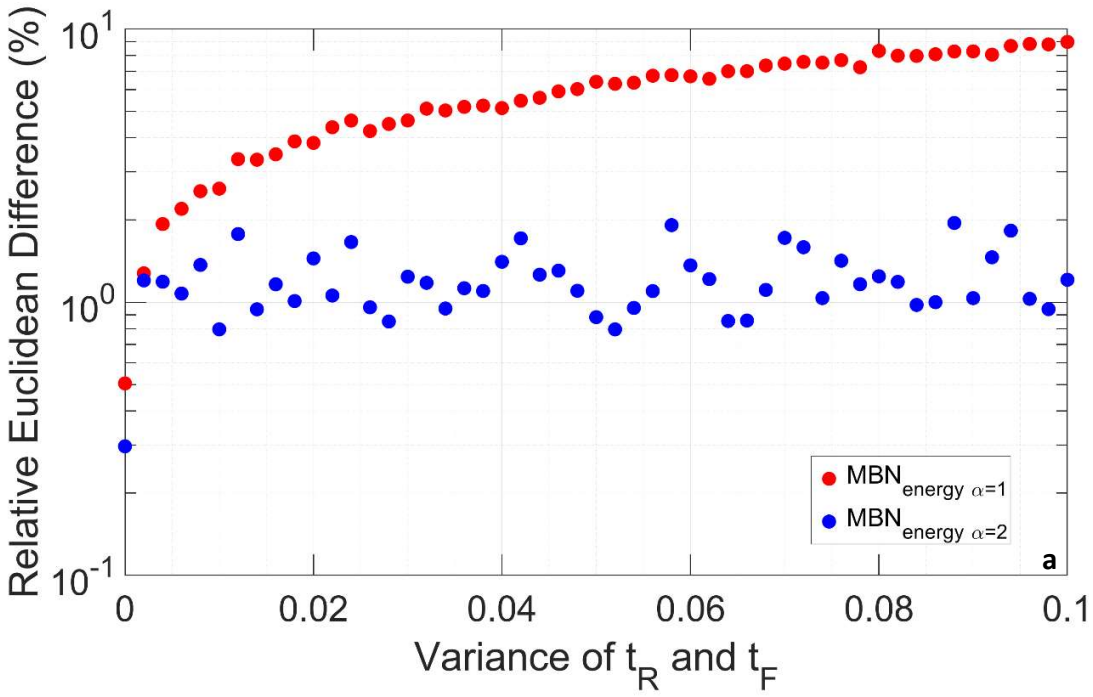

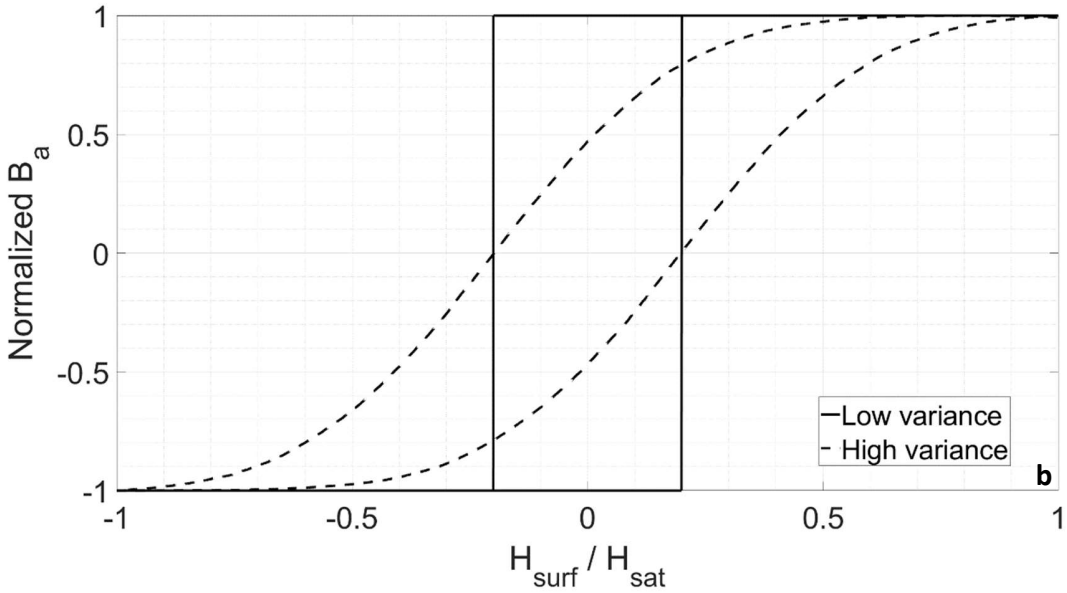

Fig. 13 – a Relative Euclidean Distance for $MBN_{energy\ \alpha=1}$ and $MBN_{energy\ \alpha=2}$ vs. variance of t_R and t_F. Fig. 13 – b $B_a(H_{surf})$ loops obtained with no time variance and significant time variance for t_R and t_F.

Conclusions regarding the experimental results can be drawn from these numerical predictions:

- Let us consider a given number of elementary events. A decrease in excitation frequency decreases the probability of superimposition. Eventually, a frequency threshold can be reached where $MBN_{energy\ \alpha=1}$ and $MBN_{energy\ \alpha=2}$ would have a similar precision. Such a frequency level would be low enough to allow individual Barkhausen jumps observation, very far from current experimental measurements. $MBN_{energy\ \alpha=2}$ is a better approximation of B_a in most cases.
- In the experimental conditions of Fig. 2, magnetization in thicker specimens will generate more elementary events, leading again to a better approximation of B_a by $MBN_{energy\ \alpha=2}$.
- In the case of low-permeability materials, the Barkhausen activity is supposed to last longer. Here again, $MBN_{energy\ \alpha=2}$ should correctly approximate B_a, as shown by Fig. 13 – a.

3 – Experimental investigation

The $B_a(H_{surf})$ hysteresis cycle is the most appropriate way to characterize a ferromagnetic material [31]. It provides direct access to the magnetic specificity of a tested specimen. International standards precisely describe the experimental conditions for reproducible and comparable $B_a(H_{surf})$ cycles. Below a frequency threshold (tens of mHz for metallic ferromagnetic materials [32][33]), the hysteresis cycle becomes frequency-independent. Here, the hysteresis area (equivalent to the energy loss during the magnetization process) is uniquely due to the microscopic eddy current associated with the domain wall motions kinetic [34].

MBN also originates from the microscopic flux variations associated with magnetic domain wall irreversible motions. By reconstructing a hysteresis cycle from the MBN raw signal, including an integration step, one can expect similarities in the shape of the hysteresis cycles. This assumption seems especially valid for strongly anisotropic materials characterized by high magneto-crystalline coefficients and a limited magnetization rotation contribution [20].

In the previous section, we have theoretically demonstrated that Ba(Hsurf) and $MBN_{energy\ \alpha=2}$(Hsurf) are expected to be similar in the absence of magnetization rotation and standard experimental conditions. This section describes an experimental investigation of the MBN_{energy}(Hsurf) hysteresis cycles, trying to confirm these statements. A series of representative materials were studied. Classical and Barkhausen noise cycles were plotted from electrical signals monitored simultaneously and in the same experimental conditions (same sensors, same inductors), and conclusions were drawn.

3.1 – Tested specimens

Table 3 lists the tested specimens and some of their magnetic properties.

	Thickness (mm)	Density (kg·dm^{-3})	Resistivity (µΩ·cm)	Core loss - 50 Hz (W·kg-1)		Min. mag. Flux dens. at 5000 A·m^{-1} (T)	Coercivity (A·m^{-1})
				1T	1.5T		
Oriented grain electrical steel - GO FeSi	0.35	7.65	47	-	1.05	-	25
Oriented grain electrical steel - NO FeSi	0.35	7.65	47	1.02	2.3	1.67	40
Iron Cobalt	0.23	8.12	40	-	-	-	185
Low carbon steel	0.6	7.85	15	2.5	6	-	160

Tab. 3 – Tested specimens list and some of their magnetic properties.

These materials have been selected for their diversity and availability. They are model materials that can be considered reference materials covering many applications. Electrical steels are, for instance, omnipresent in electrical energy conversion. GO FeSi is very soft; it has a firm texture and anisotropic magnetic properties. NO FeSi is significantly more isotropic. Iron Cobalt has a low magneto-crystalline anisotropy. It is characterized by a strong influence of the rotation contribution on the $B_a(H_{surf})$ hysteresis cycle [20][35]. Finally, low-carbon steel has been chosen for its omnipresence in the industry.

3.2 – Characterization setup

An experimental setup was built to provide the magnetic signatures. The same experimental conditions (inductor, sensors, controllers) were kept for all tests. The IEC 60404-3 standard describes a single sheet tester to characterize an electrical steel lamination [35]. This standard imposes very restrictive geometrical conditions. Barkhausen noise measurement conditions didn't leave enough space, and the double yoke we used slightly differed from the standard description. Still, our setup (Fig. 14) has been conceived by taking inspiration from [35].

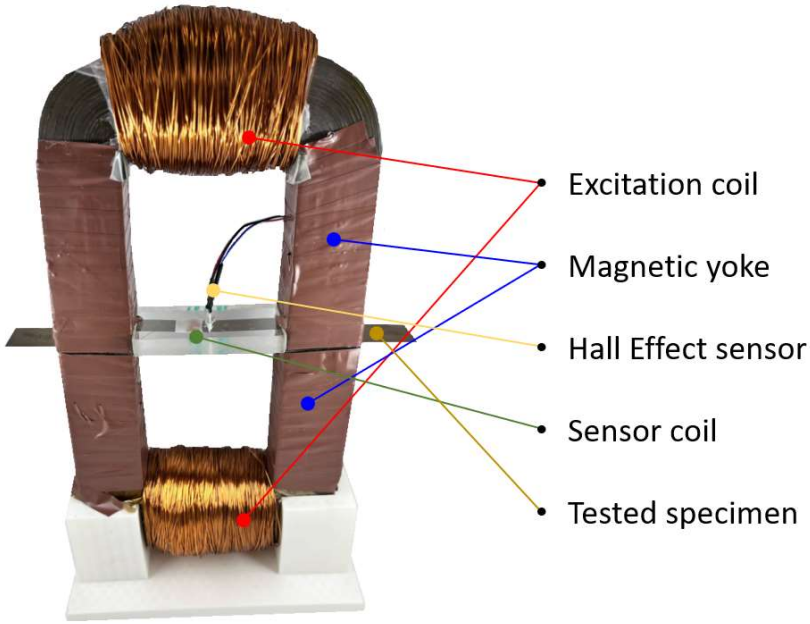

Fig. 14 – Experimental setup illustration.

3.2.1 - Magnetic excitation

The magnetic inductor was made of two U-shaped FeSi 3 wt.% yokes. The leg size of the yokes was 37 mm × 37 mm, and the inner distance between the legs was 69 mm. The excitation coil was wound around the yoke and supplied by a power amplifier (HSA 4014, NF Corporation,

Yokohama, Japan) driven by a frequency generator (Agilent 33220A, Santa Clara, CA, USA) with a 0.01 Hz sinus waveform.

3.2.2 – $B_a(H_{surf})$ hysteresis cycles

The tangent magnetic field H_{surf} was measured locally on the surface of the tested specimens in the field direction using a hall element sensor (SS94A, Honeywell, Charlotte, NC, USA). The magnetic response of the hall element was pre-characterized using a Helmholtz coil driven by a current source in a DC mode.

All the tested specimens were wrapped with an n = 100 turns sensor coil. The voltage drop due to the magnetization variations was recorded using an oscilloscope (Tektronix, Beaverton, Oregon, USA). B_a was obtained by numerical integration (Eq. 2, where S is the cross-section, and e is the sensor coil electromotive force). A post-processing correction was done to remove the undesired drift due to the ambient noise.

$$B_a(t) = -\frac{1}{n \cdot S}\int_0^t e(t)dt \tag{54}$$

3.2.3 – $MBN_{energy}(H_{surf})$ hysteresis cycles

The MBN_{energy} quantity was returned by combining analog and numerical procedures:

- The sensor coil raw electromotive force was filtered and amplified using a Stanford Research SR650 (Sunnyvale, CA, USA). The high-pass filter cut-off frequency was set to 1 kHz, and the gain to 60 $dB \cdot dec^{-1}$. No low-pass filter was used. All signals were recorded using a Sirius® acquisition card (Dewesoft, Slovenia) with a 2 MHz sampling frequency.

- The analytical treatments (square, absolute value, integration, drift correction, etc.) were done numerically using Matlab® software.

Besides raw MBN, All the data were averaged over four excitation periods to reduce the parasitic noises.

3.3 – Experimental results

As recalled in the introduction, MBN_{energy} can be assimilated as an image of the domain walls' kinetic energy. It can also be considered proportional to the irreversible contribution of magnetization. It is, however, not a flux density, and the only way to compare $MBN_{energy}(H_{surf})$ and the standard $B_a(H_{surf})$ hysteresis loops has to go through a renormalization. For this renormalization, we tested two options (Fig. 15):

- Equalizing the hysteresis areas, assuming the domain wall motions as fully responsible for the hysteresis loss contribution.
- Equalizing the MBN_{energy} and the B_a levels when the saturation elbow is reached, i. e. when magnetization rotation is supposed to start. In this option, magnetization rotation can be a source of loss. There is, unfortunately, no standard definition for the beginning of the saturation point. Then we considered H_{surf} at the "saturation point" reached when $\mu_{diff\ inc} = 0.8 \cdot \mu_{diff\ Hc}$ ($\mu_{diff\ inc}$ is the differential permeability of the hysteresis loop increasing branch, and $\mu_{diff\ Hc}$ the differential permeability at coercivity). This definition remains arbitrary, but the final results are expected to be close anyway.

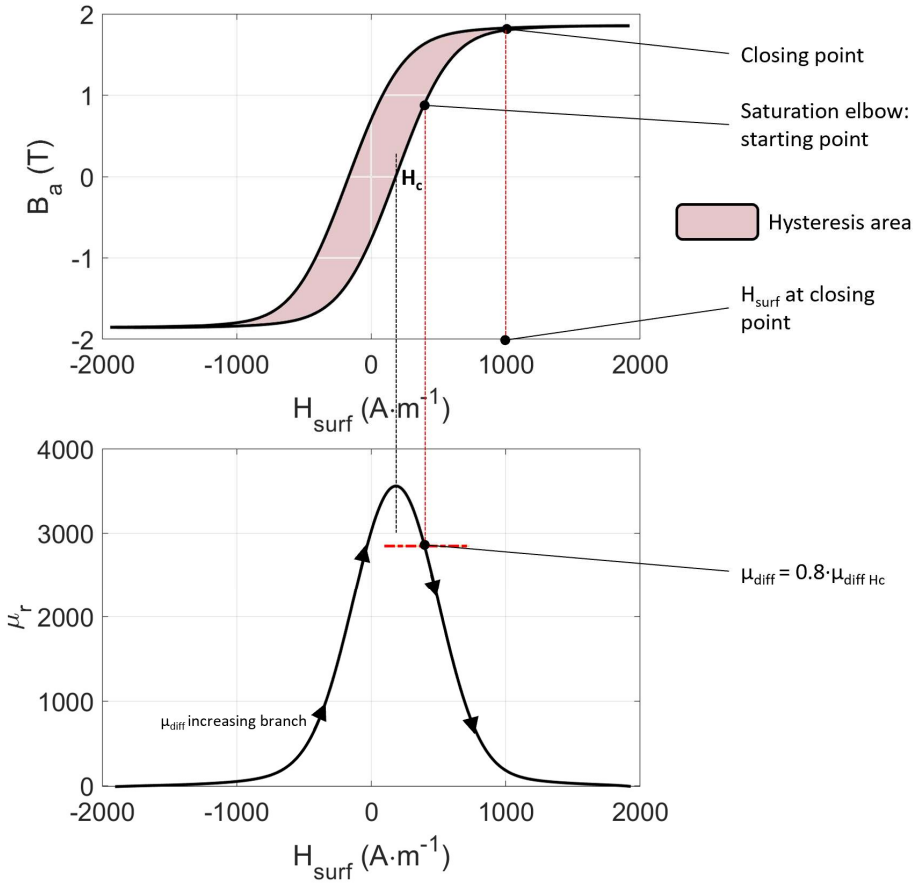

Fig. 15 – Renormalization option illustrations.

Fig. 16, 17, 18, and 19 depict all experimental results, including comparisons between the MBN cycles before and after the renormalization processes. Table 4 gives the level of similitude between classical and MBN cycles based on the Relative discrete Euclidean Difference (RED) as defined in Eq. 3:

$$RED_{discrete}\ (\%) = 100 \cdot \sqrt{\frac{\sum_{i=1}^{m} \left| x_i^{MBN} - x_i^{clas} \right|^2}{\sum_{i=1}^{m} \left| x_i^{clas} \right|^2}} \tag{55}$$

A 0% error is reached when the classical and MBN cycles perfectly match. All measured hysteresis cycles are supposed to be symmetrical; thus, we limited the application of the error function to the increasing part of the cycle.

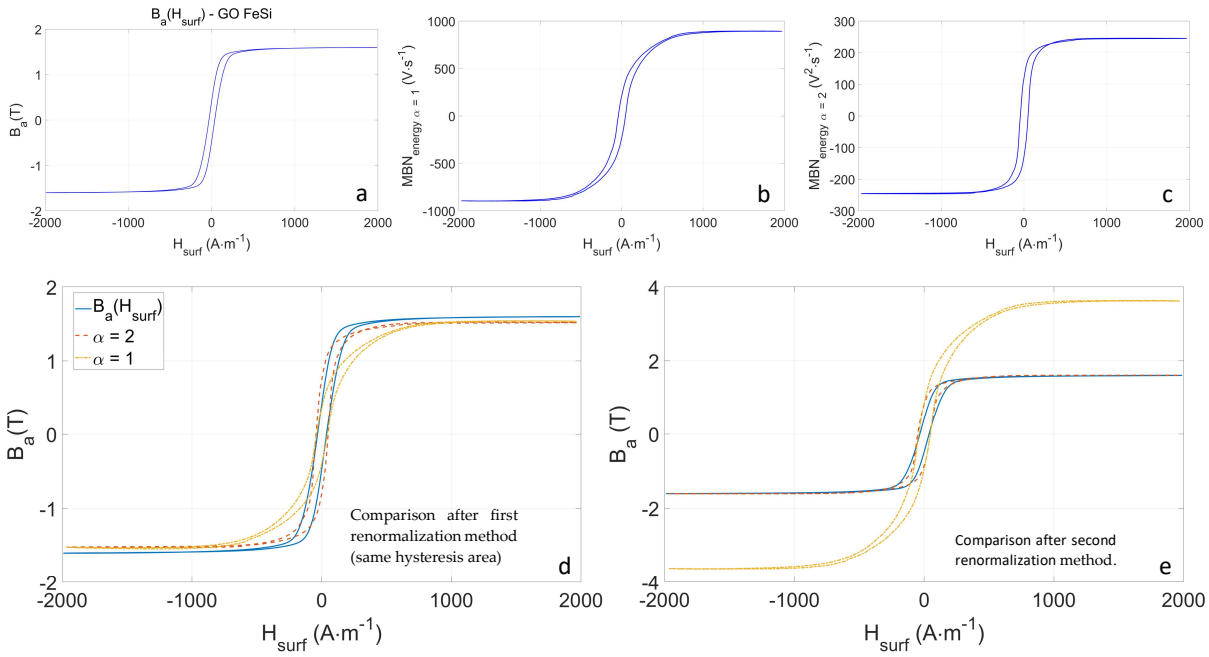

Fig. 16 – a GO FeSi $B_a(H_{surf})$ hysteresis cycle. Fig. 16 – b GO FeSi $MBN_{energy\ \alpha = 1}(H_{surf})$ hysteresis cycle. Fig. 16 – c GO FeSi $MBN_{energy\ \alpha = 2}(H_{surf})$ hysteresis cycle. Fig. 16 – d Comparison GO FeSi $B_a(H_{surf})/MBN_{energy}(H_{surf})$ hysteresis cycles after the first renormalization method (same hysteresis area). Fig. 16 – e Comparison GO FeSi $B_a(H_{surf})/MBN_{energy}(H_{surf})$ hysteresis cycles after the second renormalization method.

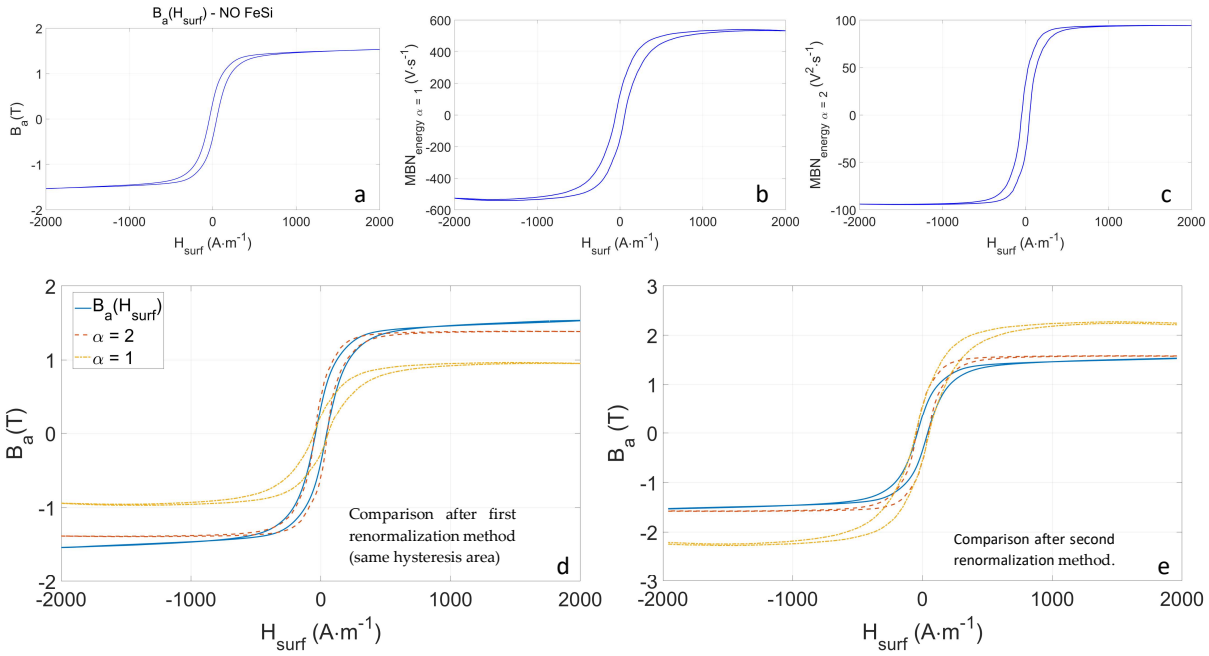

Fig. 17 – a NO FeSi $B_a(H_{surf})$ hysteresis cycle. Fig. 17 – b NO FeSi $MBN_{energy\ \alpha = 1}(H_{surf})$ hysteresis cycle. Fig. 17 – c NO FeSi $MBN_{energy\ \alpha = 2}(H_{surf})$ hysteresis cycle. Fig. 17 – d Comparison NO FeSi $B_a(H_{surf})/MBN_{energy}(H_{surf})$ hysteresis cycles after the first renormalization method (same hysteresis area). Fig. 17 – e Comparison NO FeSi $B_a(H_{surf})/MBN_{energy}(H_{surf})$ hysteresis cycles after the second renormalization method.

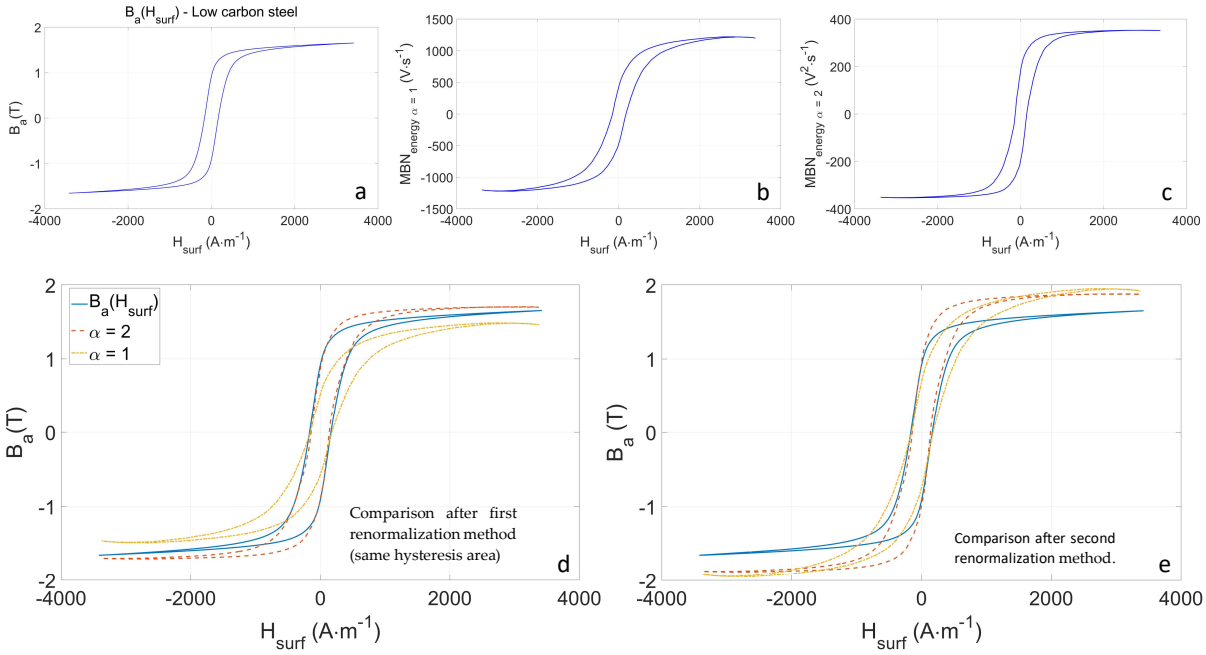

Fig. 18 – a Low carbon steel $B_a(H_{surf})$ hysteresis cycle. Fig. 18 – b Low carbon steel $MBN_{energy\ \alpha = 1}(H_{surf})$ hysteresis cycle. Fig. 18 – c Low carbon steel $MBN_{energy\ \alpha = 2}(H_{surf})$ hysteresis cycle. Fig. 18 – d Comparison Low carbon steel $B_a(H_{surf})/MBN_{energy}(H_{surf})$ hysteresis cycles after the first renormalization method (same hysteresis area). Fig. 18 – e Comparison Low carbon steel $B_a(H_{surf})/MBN_{energy}(H_{surf})$ hysteresis cycles after the second renormalization method.

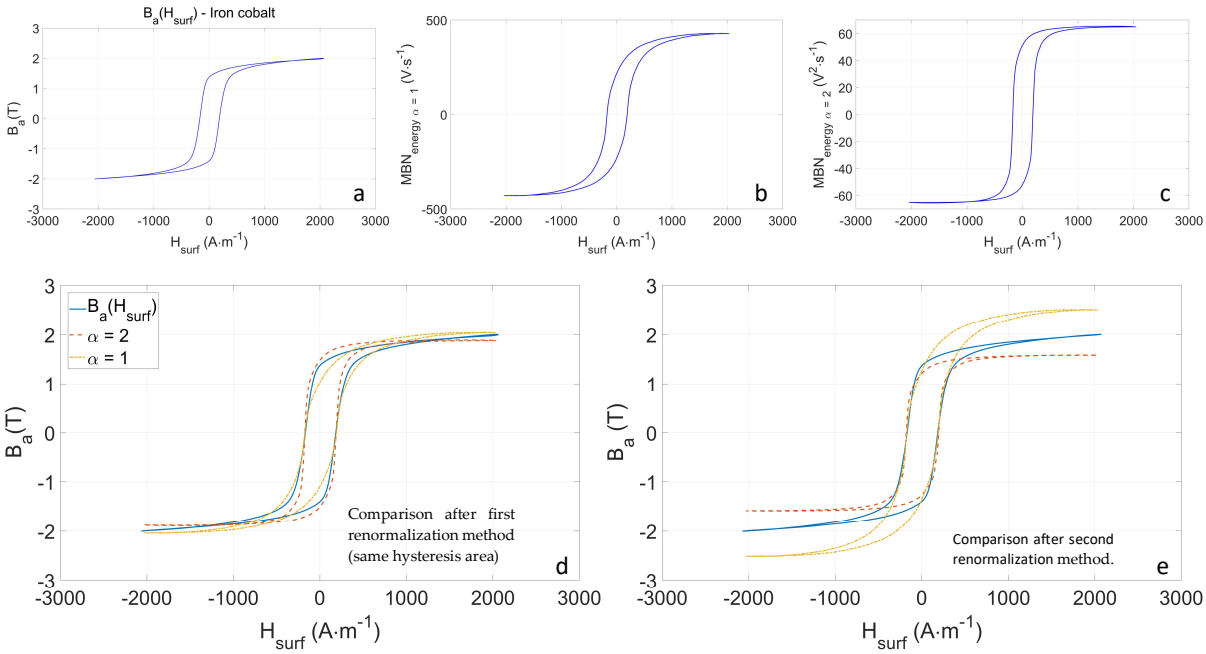

Fig. 19 – a Iron cobalt $B_a(H_{surf})$ hysteresis cycle. Fig. 19 – b Iron cobalt $MBN_{energy\ \alpha = 1}(H_{surf})$ hysteresis cycle. Fig. 19 – c Iron cobalt $MBN_{energy\ \alpha = 2}(H_{surf})$ hysteresis cycle. Fig. 19 – d Comparison iron cobalt $B_a(H_{surf})/MBN_{energy}(H_{surf})$ hysteresis cycles after the first renormalization method (same hysteresis area). Fig. 19 – e Comparison iron cobalt $B_a(H_{surf})/MBN_{energy}(H_{surf})$ hysteresis cycles after the second renormalization method.

		Renormalization option 1	Renormalization option 2
GO FeSi	α = 1	11.74 %	117.44 %
	α = 2	6.17 %	9.35 %
NO FeSi	α = 1	37.22 %	48.19 %
	α = 2	6.66 %	9.24 %
Low carbon steel	α = 1	14.91 %	19.9 %
	α = 2	8.43 %	16.3 %
Iron cobalt	α = 1	46.82 %	52.53 %
	α = 2	41.17 %	45.28 %

Tab. 4 – Comparisons in the error level between $B_a(H_{surf})$ and $MBN_{energy}(H_{surf})$ cycles for the two renormalization options based on the relative discrete Euclidean difference.

3.4 – Discussion

In the range of magnetic field amplitudes tested in the study, the magnetization rotation is supposed to have a minor influence on the hysteresis cycle shape of materials characterized by high magnetocrystalline coefficients. This category of materials includes the GO and the NO electrical steels. Indeed, even if the silicon or the carbon adjunction reduces the magnetocrystalline coefficients, electrical and low-carbon steel's magnetocrystalline coefficients remain much higher than the iron-cobalt ones. Once the renormalization is made, the resulting RED should be low for these materials. The specific texture of FeSi GO should emphasize this effect by creating even stronger magnetic anisotropic properties.

Table 4 confirms this statement with lower RED for the electrical steel materials. Oppositely, the Iron-Cobalt, shows a relatively high RED, especially for the first renormalization option, which is the best overall.

Now, let's consider the GO FeSi as the material giving the closest experimental conditions to those of the theoretical development (absence of magnetization rotation). $MBN_{energy\ \alpha=2}(H_{surf})$ cycles are for both renormalization options more comparable to the $B_a(H_{surf})$, confirming the theoretical conclusions.

Still, no perfect match can be seen, meaning that magnetization rotation contribution is never entirely negligible.

4 – Conclusion

The raw MBN signal is unpredictable and quasi-impossible to interpret. In the industry, it is always substituted by a time-average quantity like the envelope, the Root Mean Square value, or the MBN_{energy}. The latter has been studied in this paper. A hysteresis cycle can be obtained by plotting MBN_{energy} as a function of $H_{surf.}$ The link between this cycle and the classical $B_a(H_{surf})$ one is the open question we tried to answer in this study.

A theoretical development was proposed in the first part of the manuscript. A model based on elementary magnetization variations was described for reconstructing the $B_a(H_{surf})$ and $MBN_{energy}(H_{surf})$ hysteresis curves. B_a was obtained assuming all elementary variations in the same direction and $MBN_{energy}(H_{surf})$ with an isotropic angle distribution. The magnetization rotation contribution was not considered, and the hysteresis contribution was limited to the domain wall motions.

The square and the proportional relations were tested for the $MBN_{energy}(H_{surf})$ cycles. A close behavior between the classical hysteresis and the $MBN_{energy\ \alpha=2}(H_{surf})$ cycles was predicted for homogeneous magnetization distribution, a significant number of Barkhausen events, and a not-too-stiff hysteresis shape.

Then, experimental tests on model materials were run and confirmed the simulation prediction and the possibility of isolating the hysteresis contribution associated with the domain wall motions using the $MBN_{energy\ \alpha\ =\ 2}(H_{surf})$ cycle. Two renormalization options were proposed for a direct comparison with the $B_a(H_{surf})$ cycles, and good results were obtained by basing this renormalization on the hysteresis area.

Still, open questions remain and constitute perspectives for this work; those include the signal seen by the Barkhausen noise sensor, as pointed out in recent papers [36][37]. Assessing this issue would help complete the renormalization of the $MBN_{energy}(H_{surf})$ hysteresis cycle and confirm the conclusions of this study. Also, all experimental tests were done using a wrapped coil. Such sensors are impossible to implement in an NDT situation and are always replaced with a surface coil. Validating the results independency vs. the MBN sensor constitutes another exciting perspective.

References

[1] Spasojević, D., Bukvić, S., Milošević, S. and Stanley, H.E., 1996. Barkhausen noise: Elementary signals, power laws, and scaling relations. *Physical Review E*, *54*(3), p.2531.

[2] Le Manh, T., Benitez, J.A.P., Hernandez, J.H.E. and Hallen, J.M. eds., 2020. *Barkhausen Noise for Non-destructive Testing and Materials Characterization in Low Carbon Steels*. Woodhead Publishing.

[3] Desvaux, S., Duquennoy, M., Gualandri, J. and Ourak, M., 2004. The evaluation of surface residual stress in aeronautic bearings using the Barkhausen noise effect. *NDT & E International*, *37*(1), pp.9-17.

[4] Le Manh, T., Benitez, J.A.P. and Alberteris, M., 2020. Future trend and applications of Barkhausen noise. In *Barkhausen Noise for Non-destructive Testing and Materials Characterization in Low-Carbon Steels* (pp. 239-253). Woodhead Publishing.

[5] Santa-Aho, S., Vippola, M., Sorsa, A., Latokartano, J., Lindgren, M., Leiviskä, K. and Lepistö, T., 2012. Development of Barkhausen noise calibration blocks for reliable grinding burn detection. *Journal of Materials Processing Technology*, *212*(2), pp.408-416.

[6] Moorthy, V., Shaw, B.A. and Evans, J.T., 2003. Evaluation of tempering induced changes in the hardness profile of case-carburised EN36 steel using magnetic Barkhausen noise analysis. *Ndt & E International*, *36*(1), pp.43-49.

[7] Gauthier, J., Krause, T.W. and Atherton, D.L., 1998. Measurement of residual stress in steel using the magnetic Barkhausen noise technique. *Ndt & E International*, *31*(1), pp.23-31.

[8] Ducharne, B., Gupta, B., Hebrard, Y. and Coudert, J.B., 2018. Phenomenological model of Barkhausen noise under mechanical and magnetic excitations. *IEEE Transactions on Magnetics*, *54*(11), pp.1-6.

[9] Bozorth, R.M., 1951. Ferromagnetism, fac-simile reissue.

[10] Cullity, B.D. and Graham, C.D., 2011. *Introduction to magnetic materials*. John Wiley & Sons.

[11] Hornreich, R., Rubinstein, H. and Spain, R., 1971. Magnetostrictive phenomena in metallic materials and some of their device applications. *IEEE Transactions on Magnetics*, *7*(1), pp.29-48.

[12] Urbach, J.S., Madison, R.C. and Markert, J.T., 1995. Reproducibility of magnetic avalanches in an Fe-Ni-Co ferromagnet. *Physical review letters*, *75*(25), p.4694.

[13] Petta, J.R., Weissman, M.B. and Durin, G., 1997. Dependence of Barkhausen pattern reproducibility on hysteresis loop size. *Physical Review E*, *56*(3), p.2776.

[14] Sakamoto, H., Okada, M. and Homma, M., 1987. Theoretical analysis of Barkhausen noise in carbon steels. *IEEE transactions on magnetics*, *23*(5), pp.2236-2238.

[15] Samimi, A.A., Krause, T.W. and Clapham, L., 2016. Multi-parameter evaluation of magnetic Barkhausen noise in carbon steel. *Journal of Non-destructive Evaluation*, *35*(3), pp.1-8.

[16] Krause, T.W., Clapham, L. and Atherton, D.L., 1994. Characterization of the magnetic easy axis in pipeline steel using magnetic Barkhausen noise. *Journal of Applied Physics*, *75*(12), pp.7983-7988.

[17] Jiles, D.C., Sipahi, L.B. and Williams, G., 1993. Modeling of micromagnetic Barkhausen activity using a stochastic process extension to the theory of hysteresis. *Journal of applied physics*, *73*(10), pp.5830-5832.

[18] Dhar, A., Clapham, L. and Atherton, D.L., 2001. Influence of uniaxial plastic deformation on magnetic Barkhausen noise in steel. *Ndt & E International*, *34*(8), pp.507-514.

[19] Ducharne, B., Le, M.Q., Sebald, G., Cottinet, P.J., Guyomar, D. and Hebrard, Y., 2017. Characterization and modeling of magnetic domain wall dynamics using reconstituted hysteresis loops from Barkhausen noise. *Journal of Magnetism and Magnetic Materials*, *432*, pp.231-238.

[20] Fagan, P., Ducharne, B., Daniel, L. and Skarlatos, A., 2021. Multiscale modelling of the magnetic Barkhausen noise energy cycles. *Journal of Magnetism and Magnetic Materials*, *517*, p.167395.

[21] Fagan, P., Ducharne, B., Daniel, L., Skarlatos, A., Domenjoud, M. and Reboud, C., 2022. Effect of stress on the magnetic Barkhausen noise energy cycles: A route for stress evaluation in ferromagnetic materials. *Materials Science and Engineering: B*, *278*, p.115650.

[22] Meng, X., Li, L. and Hou, Y., 2022. Construction of Energy Loops Using Magnetic Barkhausen Noise. *IEEE Magnetics Letters*, *13*, pp.1-5.

[23] Jiles, D.C. and Atherton, D.L., 1986. Theory of ferromagnetic hysteresis. *Journal of magnetism and magnetic materials*, *61*(1-2), pp.48-60.

[24] Bertotti, G., 1987. Dynamics of magnetic domain walls and Barkhausen noise in metallic ferromagnetic systems. In *Magnetic Excitations and Fluctuations II* (pp. 135-139). Springer, Berlin, Heidelberg.

[25] Alessandro, B., Beatrice, C., Bertotti, G. and Montorsi, A., 1990. Domain-wall dynamics and Barkhausen effect in metallic ferromagnetic materials. I. Theory. *Journal of applied physics*, *68*(6), pp.2901-2907.

[26] Jiles, D.C., Sipahi, L.B. and Williams, G., 1993. Modeling of micromagnetic Barkhausen activity using a stochastic process extension to the theory of hysteresis. *Journal of applied physics*, *73*(10), pp.5830-5832.

[27] Ducharne, B., Deffo, Y.T., Tsafack, P. and Kouakeuo, S.N., 2021. Directional magnetic Barkhausen noise measurement using the magnetic needle probe method. *Journal of Magnetism and Magnetic Materials*, *519*, p.167453.

[28] Bertotti, G., Fiorillo, F., & Soardo, G. P. (1988). The prediction of power losses in soft magnetic materials. *Le Journal de Physique Colloques*, *49*(C8), C8-1915.

[29] Rumbos, A.J., 2008. “Probability – Lecture Notes”, p. 47-49.

[30] Ortega-Labra, O., Martinez-Ortiz, P., Le Manh, T., Velazquez-Lozada, E., Perez-Benitez, J.A., 2022, What does a Barkhausen surface coil actually measure? *Journal of Magnetism and Magnetic Materials*, *563*, p.169938.

[31] Bertotti, G., 1998. *Hysteresis in magnetism: for physicists, materials scientists, and engineers*. Gulf Professional Publishing.

[32] Zhang, S., Ducharne, B., Takeda, S., Sebald, G. and Uchimoto, T., 2021. Low-frequency behavior of laminated electric steel sheet: investigation of ferromagnetic hysteresis loops and incremental permeability. *Journal of Magnetism and Magnetic Materials*, *538*, p.168278.

[33] Bertotti, G., 1985. Physical interpretation of eddy current losses in ferromagnetic materials. I. Theoretical considerations. *Journal of applied Physics*, *57*(6), pp.2110-2117.

[34] Toutsop, B., Ducharne, B., Lallart, M., Morel, L. and Tsafack, P., 2022. Characterization of Tensile Stress-Dependent Directional Magnetic Incremental Permeability in Iron-Cobalt Magnetic Sheet: Towards Internal Stress Estimation through Non-Destructive Testing. *Sensors*, *22*(16), p.6296.

[35] IEC 60404-3; Magnetic Materials—Part 3: Methods of Measurement of the Magnetic Properties of Electrical Strip and Sheet by Means of a Single Sheet Tested. International Electrotechnical Commission: Geneva, Switzerland, 2010.

[36] Stupakov, A., Perevertov, A. and Neslušan, M., 2020. Reading depth of the magnetic Barkhausen noise. I. One-phase semi-hard ribbons. *Journal of Magnetism and Magnetic Materials*, *513*, p.167086.

[37] Stupakov, A., Perevertov, A. and Neslušan, M., 2020. Reading depth of the magnetic Barkhausen noise. II. Two-phase surface-treated steels. *Journal of Magnetism and Magnetic Materials*, *513*, p.167239.

[38] Stupakov, A., 2019. Dynamic normalization of the Barkhausen noise signal. *Journal of Magnetism and Magnetic Materials*, *482*, pp.135-147.

Annexes

1. Eq. 24: theoretical development

This annex provides additional analytical developments associated with Eq. 24. The general case is treated first. The distribution of sinus ϕ is called D and is defined as follows:

$$D_i = sin\ \phi_i \tag{A.1}$$

The average μ_D and the standard deviation σ_D are supposedly defined and strongly linked to the PDF of Φ.

Eq. (24) can be developed like:

$$V_{MBN}(t) = \frac{\mu_0}{N_d} \sum_{i \in X(t)} D_i \tag{A.2}$$

Since Φ_i have a random distribution, they won't be regularly spaced between $-\frac{\pi}{2}$ and $\frac{\pi}{2}$. Therefore, the sum is not null, even in the isotropic case. This result is not intuitive, considering that $\int_{-\frac{\pi}{2}}^{\frac{\pi}{2}} sin\theta d\theta = 0$.

Instead, applying the CLT to the distribution D gives:

$$\sqrt{N}\left(\frac{\sum_{i=1}^{N} D_i}{N} - \mu_D\right) \to \mathcal{N}(0;\ \sigma_D^2) \tag{A.3}$$

Fig. 20 gives an example. Here, 10^5 samples have been extracted from $\frac{\sum_{i=1}^{N} D_i}{N}$ (the normalized version of D) for $N=10^4$ and compared to the theoretical normal distribution calculated thanks to the CTL. The correspondence between the two distributions is remarkable.

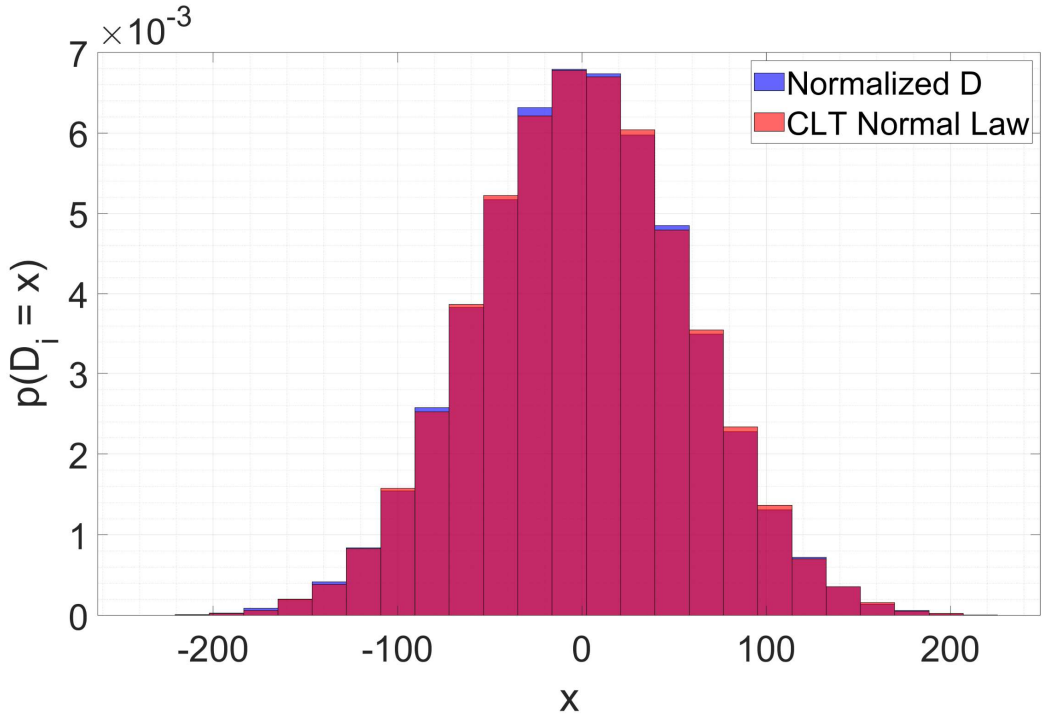

Fig. 20 – Comparison between the normalized sum of sin Φ_i PDF and the CLT normal distribution.

By applying the CLT, V_{MBN} can be written as follows:

$$V_{MBN}(t) = \frac{\mu_0}{N_d} \sum_{i \in X(t)} D_i \tag{A.4}$$

$$= \frac{\mu_0}{N_d} \cdot \left[\sum_{i \in X(t)} D_i - \bar{\bar{X}}(t)\mu_D + \bar{\bar{X}}(t)\mu_D\right]$$

$$= \frac{\mu_0}{N_d} \cdot \bar{\bar{X}}(t) \cdot \left[\frac{\sum_{i \in X(t)} D_i - \bar{\bar{X}}(t)\mu_D}{\bar{\bar{X}}(t)} + \mu_D\right]$$

$$= \frac{\mu_0}{N_d} \cdot \sqrt{\bar{\bar{X}}(t)} \cdot \left\{\sqrt{\bar{\bar{X}}(t)}\left[\frac{\sum_{i \in X(t)} D_i}{\bar{\bar{X}}(t)} - \mu_D\right]\right\} + \frac{\mu_0}{N_d}\bar{\bar{X}}(t)\,\mu_D$$

$$V_{MBN}(t) = \frac{\mu_0}{N_d} \cdot \sqrt{\bar{\bar{X}}(t)} \cdot \mathcal{N}(0;\, \sigma_D^2) + \frac{\mu_0}{N_d}\bar{\bar{X}}(t)\,\mu_D \tag{A.5}$$

In the general case, V_{MBN} becomes a deterministic term depending on the number of active events $\bar{\bar{X}}(t)$, the average of D, and a stochastic term following a normal law multiplied by the square root of $\bar{\bar{X}}(t)$. $MBN_{energy\ \alpha=1}$ is obtained by integrating the absolute value of V_{MBN}:

$$|V_{MBN}(t)| = \frac{\mu_0}{N_d} \cdot \sqrt{\bar{\bar{X}}(t)} \cdot \left| \mathcal{N}(0;\, \sigma_D^2) + \mu_D \sqrt{\bar{\bar{X}}(t)} \right| \tag{A.6}$$

$$= \frac{\mu_0}{N_d} \cdot \sqrt{\bar{\bar{X}}(t)}\, F_{\mathcal{N}}\left(\mu_D \sqrt{\bar{\bar{X}}(t)}; \sigma_D^2\right)$$

Where $F_{\mathcal{N}}$ is the folded normal law of the location $\mu_D \sqrt{\bar{\bar{X}}(t)}$ and scale σ_D^2.

If the angle distribution is symmetrical on the z-axis (which includes the isotropic case), then $\mu_D = 0$, and the above equations can be simplified:

$$V_{MBN}(t) = \frac{\mu_0}{N_d} \cdot \sqrt{\bar{\bar{X}}(t)} \cdot \mathcal{N}(0;\, \sigma_D^2) \tag{A.7}$$

$$|V_{MBN}(t)| = \frac{\mu_0}{N_d} \cdot \sqrt{\bar{\bar{X}}(t)}\, F_{\mathcal{N}}(0; \sigma_D^2) \tag{A.8}$$

The folded normal law is simplified by a half-normal law, whose average and standard deviation are given by:

$$\mu_F = \sigma_D \sqrt{\frac{2}{\pi}} \tag{A.9}$$

$$\sigma_F = \sigma_D \sqrt{1 - \frac{2}{\pi}} \tag{A.10}$$

The angle distribution is supposed to be uniform in time. After averaging on several cycles, one can expect $IV_{MBN}I$ to be proportional to the square root of $\bar{\bar{X}}(t)$ (and dB_a/dt):

$$\overline{|V_{MBN}(t)|} = \frac{\mu_0}{N_d} \cdot \sqrt{\bar{\bar{X}}(t)}\, \sigma_D \sqrt{\frac{2}{\pi}} = \sigma_D \sqrt{\frac{2}{\pi}} \sqrt{\left|\frac{dB_a}{dt}\right|} \tag{A.11}$$

In conclusion, as long as the angle distribution is symmetrical on the z-axis, $MBN_{energy\ \alpha=2}$ will approach better B_a rather than $MBN_{energy\ \alpha=1}$, since the latter is proportional to $\sqrt{\left|\frac{dB_a}{dt}\right|}$.

For the isotropic case (Eq. 15), we have $\sin(\phi_i) = \sin\left[\text{asin}\left(2R_{2_i} - 1\right)\right] = 2R_{2_i} - 1$, where D is a uniform random law between +1 and -1, hence:

$$\sigma_D^2 = \frac{[1-(-1)]^2}{12} = \frac{1}{3} \quad \text{(A.12)}$$

Here, the proportionality coefficient can be calculated analytically:

$$\overline{|V_{MBN}(t)|} = \sqrt{\frac{1}{3}\frac{2}{\pi}}\sqrt{\left|\frac{dB_a}{dt}\right|} \approx 0.461\sqrt{\left|\frac{dB_a}{dt}\right|} \quad \text{(A.13)}$$

2. Analytical expression of μ_A and μ_B in the isotropic case

This annex provides additional developments for calculating the analytical expression of μ_A and μ_B in the isotropic case (sub-section 3.2.1 in the text).

Let us consider a random variable X with probability distribution function p_X. The PDF p_Y of a related random variable y defined by $y = g(x)$ (with g a monotonic increasing function) can be calculated as:

$$p_Y(y) = p_X[g^{-1}(y)] \cdot \frac{1}{g'[g^{-1}(y)]} \quad \text{(A.14)}$$

The distribution of ϕ being defined in Eq. 14, one can, step by step, calculate the PDF of A, p_A:

$$p_{R_2}(r_2) = \begin{cases} 1 & if\ r_2 \in [0;1] \\ 0 & otherwise \end{cases} \quad \text{(A.15)}$$

$$R = 2R_2 - 1 = g(R_2) \Rightarrow g'(r_2) = 2 \quad \text{(A.16)}$$

$$r = 2r_2 - 1 \Rightarrow r_2 = \frac{r+1}{2}$$

Leading to:

$$p_R(r) = p_{R_2}\left(\frac{r+1}{2}\right) \cdot \frac{1}{g'\left(\frac{r+1}{2}\right)} \quad \text{(A.17)}$$

$$p_R(r) = \begin{cases} \frac{1}{2} & if\ \frac{r+1}{2} \in [0;1] \Rightarrow r \in [-1;1] \\ 0 & otherwise \end{cases} \quad \text{(A.18)}$$

$$\Phi = asin\,(R) = g(R) \Rightarrow g'(r) = \frac{1}{\sqrt{1-r^2}} \quad \text{(A.19)}$$

$$\phi = asin(r) \Rightarrow r = sin\,(\phi)$$

$$R = 2R_2 - 1 = g(R_2) \Rightarrow g'(r_2) = 2 \quad \text{(A.20)}$$

$$r = 2r_2 - 1 \Rightarrow r_2 = \frac{r+1}{2}$$

$$p_\Phi(\phi) = p_R(sin(\phi)) \cdot \frac{1}{g'(sin(\phi))} \quad \text{(A.21)}$$

$$r = 2r_2 - 1 \Rightarrow r_2 = \frac{r+1}{2}$$

$$p_\Phi(\phi) = \begin{cases} \frac{1}{2} \cdot \frac{1}{\sqrt{1-sin^2\,\phi}} & if\ sin\,\phi \in [-1;1] \Rightarrow \phi \in \left[-\frac{\pi}{2};\frac{\pi}{2}\right] \\ 0 & otherwise \end{cases} \quad \text{(A.22)}$$

$$\Rightarrow p_\Phi(\phi) = \begin{cases} \frac{1}{2}cos\phi & if\ \phi \in [-\frac{\pi}{2};\frac{\pi}{2}] \\ 0 & otherwise \end{cases}$$

The average and the variance of Φ are given below:

$$\mu_\phi = 0; {\sigma_\phi}^2 = \frac{\pi}{8} \quad \text{(A.23)}$$

The next step consists of calculating the PDF of A:

$$A = cos(2\Phi) = g(\Phi) \Rightarrow g'(\phi) = -2sin\,(2\phi) \quad \text{(A.24)}$$

Then two cases will be studied to verify that g is monotonic and increasing: ϕ is negative in the first case and positive in the second. a belongs to [-1;1].

In the first case:

$$a = cos(2\phi)\,; \phi \leq 0 \Rightarrow \phi = -\frac{1}{2}acos(a) \quad \text{(A.25)}$$

$$p_A(a) = p_\Phi\left(-\frac{1}{2}acos(a)\right) \cdot \frac{1}{g'\left(-\frac{1}{2}acos(a)\right)} \quad \text{(A.26)}$$

$$= \frac{1}{2} cos\left(-\frac{1}{2} acos(a)\right) \cdot \frac{1}{-2\, si\ \ (-ac\ \ \ (a))}$$

$$= \frac{1}{2} cos\left(\frac{1}{2} acos(a)\right) \cdot \frac{1}{2\, sin(acos(a))}$$

$$= \frac{1}{2}\sqrt{2}\ \sqrt{1+a}\,\frac{1}{2\ \sqrt{1-a^2}}$$

$$\Rightarrow p_A(a) = \begin{cases} \frac{1}{2\sqrt{2}}\frac{1}{\sqrt{1-a}} & if\ -\frac{1}{2} acos(a) \in \left[-\frac{\pi}{2}; 0\right] \Rightarrow a \in [-1; 1] \\ 0 & otherwise \end{cases} \quad \text{(A.27)}$$

For the second case, g is monotonic but decreasing:

$$a = cos(2\phi)\,; \phi > 0 \Rightarrow \phi = \frac{1}{2} acos(a) \quad \text{(A.28)}$$

$$p_A(a) = p_\Phi\left(\frac{1}{2} acos(a)\right) \cdot \frac{1}{-g'\left(\frac{1}{2} acos(a)\right)} \quad \text{(A.29)}$$

$$= \frac{1}{2} cos\left(\frac{1}{2} acos(a)\right) \cdot \frac{1}{2\, sin(acos(a))}$$

$$= \frac{1}{2\sqrt{2}}\frac{1}{\sqrt{1-a}}$$

$$\Rightarrow p_A(a) = \begin{cases} \frac{1}{2\sqrt{2}}\frac{1}{\sqrt{1-a}} & if\ -\frac{1}{2} acos(a) \in \left[-\frac{\pi}{2}; 0\right] \Rightarrow a \in [-1; 1] \\ 0 & otherwise \end{cases} \quad \text{(A.30)}$$

Finally, the PDF, average, and variance of A are given below:

$$p_A(a) = \begin{cases} \frac{1}{2\sqrt{2}}\frac{1}{\sqrt{1-a}} & if\ a \in [-1; 1] \\ 0 & otherwise \end{cases} \quad \text{(A.31)}$$

$$\mu_A = \frac{1}{3}; {\sigma_A}^2 \approx 0.355 \quad \text{(A.32)}$$